Doctoral Dissertation

Energy consumption and production in cardiomyocytes: a new myofilament contraction model with ATP consumption and the diagnosis of ATP productive impairment from missense mutations

March 2018

Doctoral Program in Advanced Life Sciences
Graduate School of Life Sciences
Ritsumeikan University

MUANGKRAM Yuttamol

Doctoral Dissertation Reviewed

By Ritsumeikan University

Energy consumption and production in cardiomyocytes: a new myofilament contraction model with ATP consumption and the diagnosis of ATP productive impairment from missense mutations

心筋細胞におけるエネルギー消費と産生：ATP 消費を伴う新しい筋繊維収縮モデルの構築およびミスセンス変異による ATP 産生障害の診断

March 2018

2018　年　3　月

Doctoral Program in Advanced Life Sciences

Graduate School of Life Sciences

Ritsumeikan University

立命館大学大学院生命科学研究科

生命科学専攻博士課程後期課程

MUANGKRAM Yuttamol

ムガングラム　ユッタモル

Supervisor: Professor AMANO Akira

研究指導教員：天野　晃教授

Acknowledgements

I am grateful to specially thank my advisor, Professor AMANO Akira, for his valuable advisories, encouragement, constitutive, and his kindly help throughout the period of my study at Ritsumeikan University. I am also deeply to extend my sincere gratitude and appreciate to Professor NOMA Akinori for his kindness, generous guidance, and intensive supervision in conducting the research. I truly like to specially thank for “Host University Recommendation Scholarships” from Japanese Government (Monbukagakusho: MEXT) scholarship which gave me the good opportunity to study aboard, earn new experiences and learn the Japanese culture.

Energy consumption and production in cardiomyocytes: a new myofilament contraction model with ATP consumption and the diagnosis of ATP productive impairment from missense mutations

Abstract

The understanding of cardiovascular system under physiological conditions has been progressed, however, it is not fully understood. Information technology allows us to understand the complex biological mechanisms of the cardiovascular system. Since the mechanisms of crossbridge (CB) are not clearly understood, the development of CB model could provide the valuable tool to comprehend those reaction or energy consumption. A variety of CB model was constructed to explain its behavior of biological function. Nevertheless, the models that explain the necessary function that includes Ca^{2+} transient with the biochemical structure are limited. Here, we proposed a realistic model of crossbridge mechanism using mechanical model of NL model (Negroni & Lascano 1996, 2008; Negroni et al. 2015) and biochemical model of Månsson model (Månsson 2010). The model concerns with the Ca^{2+} activation and force generation assuming an equivalent crossbridge. The proposed model well reproduced the relationship of $[Ca^{2+}]$-force, length-force, $[Ca^{2+}]$-ATP hydrolysis, force generation by Ca^{2+} transient, ATPase turnover rate, force recovery after jumps in length under the isometric model and sarcomere shortening after a rapid release of mechanical load under isotonic mode with the load-velocity relation. On the other hand, mitochondrial diseases are the complex diseases associated to dysfunction or failures of the mitochondria which has a great influence in ATP production. Missense mutations in mitochondrial DNA, particularly in cytochrome *b* gene sequences in complex III have been associated with several diseases with muscle and heart. We preliminarily developed the high sensitivity and specificity technique to diagnose the mutations using PCR based sequencing. Five missense mutations in mitochondrial cytochrome *b* gene of human mitochondrial genome could be diagnosed by using the novel primers. Furthermore, the development of our techniques with high resolution melt analysis could provide the new aspect in mutation investigation at early stage.

Keywords

actomyosin-ATPase, crossbridge contraction, mechano-energetics, missense mutation diagnosis, mitochondrial mutations, myofilament model

心筋細胞におけるエネルギー消費と産生：ATP 消費を伴う新しい筋繊維収縮モデルの構築およびミスセンス変異による ATP 産生障害の診断

概要

生理学的条件下における心血管系の理解が進んでいるが、定量的な理解は不十分である。数理的な解析によって、複雑な心血管系の生理学的機構を理解が可能である。特に、筋収縮におけるクロスブリッジ(CB)の反応やエネルギー消費を明確にするため、CB モデルの開発が必要である。先行研究として、複数の CB モデルが提案されている。しかし、多くのモデルは、心機能にとって重要な役割を果たす一過性カルシウム濃度変化が導入されていない。本研究は、数理モデルである NL モデル(Negroni & Lascano 1996, 2008; Negroni et al. 2015)および生化学モデルである Månsson モデル(Månsson 2010)を用い、CB の生理学的な挙動の再現を行った。提案モデルでは、カルシウム活性と力の発生機構に、CB の平均を表わす等価 CB を用いた。提案モデルによって、$[Ca^{2+}]$-収縮力や半筋節長-収縮力、$[Ca^{2+}]$-ATP 加水分解、一過性カルシウム濃度変化による力の発生機構、ATPase の回転率、筋収縮による収縮力の回復、機械的な筋節の収縮の負荷と速度の関係を明らかにした。一方で、筋肉において重要な役割を果たす ATP 産生は、ミトコンドリアによって行われている。ATP 産生の機能不全に関連する複雑な疾患として、ミトコンドリア病がある。ミトコンドリア DNA のミスセンス変異として、特に複合体 III のシトクロム b 遺伝子が筋肉や心臓の疾患に関連がある。本研究では、PCR を用いて、高感度かつ特異的にシトクロム b 遺伝子変異を検出する技術を開発した。ヒトミトコンドリアゲノムのミトコンドリアシトクロム b 遺伝子における 5 か所のミスセンス変異が、提案のプライマーを用いることで診断可能であった。今後は、高解像度融解曲線分析を利用することで、迅速な突然変異調査に貢献することが出来ると期待される。

キーワード

アクトミオシン-ATPase、クロスブリッジ収縮、力学的エネルギー、ミスセンス変異診断、ミトコンドリア変異、筋繊維モデル

Table of contents

Table of contents (continued)

List of Tables

List of Figures

List of Figures (continued)

List of Abbreviations

A	actin filament
A6/A8	*ATP synthase 6* / *ATP synthase 8*
ADP or D	adenosine 5′-diphosphate
AM	actomyosin
A_p	parameter describing the bridge force of the power work state
ATP or T	adenosine 5′-triphosphate
A_w	parameter describing the bridge force of the weak state
B_p	parameter describing the equivalent CB kinetics of power work state
B_w	parameter describing the equivalent CB kinetics of weak state
c or Ca^{2+}	calcium
$[Ca^{2+}]_i$	intracellular calcium concentration or myoplasmic calcium concentration
Ca_{rest}	myoplasmic calcium concentration at rest
CB	crossbridge
COX	cytochrome *c* oxidase
eCB	equivalent crossbridge
f	attachment rate
FAD	flavin adenine dinucleotide
F_b	crossbridge force (total)
F_{bED}	left ventricular wall tension at end diastolic point
F_{bES}	left ventricular wall tension at end systolic point
F_{bp}	crossbridge force of power work state
F_{bw}	crossbridge force of weak state
F_{ext}	external force or load or left ventricular wall tension
FLA	force-length area
F_p	parallel elastic component force
g	detachment rate from cAM_{DPw}
γ	parameter describing Y_v detachment pathway
halfSL	half sarcomere length
h_{LV}	left ventricular wall thickness
h_{LVED}	left ventricular wall thickness at end diastolic point
h_{LVES}	left ventricular wall thickness at end systolic point
h_p	mean elongation of attached CBs in the power work state
h_{pr}	steady elongation of attached CBs in the power work state
HRM	high resolution melt
hSL0	parameter describing the parallel elastic element
HSP	promotor of transcription of the heavy strand

List of Abbreviations (continued)

h_w	mean elongation of attached CBs in the weak state
h_{wr}	steady elongation of attached CBs in the weak state
$K_{0.5}$	$[Ca^{2+}]_i$ for half maximal force in force-length-Ca^{2+} relationship
K_e	parameter describing the parallel elastic element
K_m	value of $[Ca^{2+}]$ for $Q_{pump} = K_p / 2$
K_p	maximum value of Q_{pump}
La	parameter describing attaching step
L_e	parameter describing the parallel elastic element
LSP	promotor of transcription of the light strand
M	myosin filament
[*mS1*]	the concentration of total myosin S1 segment
mtDNA	mitochondrial DNA
NAD/NADH	nicotine adenine dinucleotide
nCa	number of calcium
ND	NADH dehydrogenase
n_H	Hill coefficient in the Hill equation
O_H	origin of replication of the heavy chain
O_L	origin of replication of the light chain
PCR	polymerase chain reaction
P or P_i	inorganic phosphate
p_{LV}	left ventricular pressure
PVA	pressure-volume area
PV loop	pressure-volume loop
Q_1-Q_{13}	fluxes
Q_{10}	temperature coefficient
Q_m	maximum value of Q_{rel}
Q_{pump}	Ca^{2+} uptake flow towards the sarcoplasmic reticulum
Q_{rel}	Ca^{2+} release from the sarcoplasmic reticulum
Ra	parameter describing attaching step
r_{LV}	left ventricular radius
SERCA	sarcoplasmic reticulum Ca^{2+}-ATPases
SR	sarcoplasmic reticulum
t_1	time to Q_m
TS	troponin system
v_{ATPase}	ATP consumption rate or ATPase activity

List of Abbreviations (continued)

v_{LV}	left ventricular volume
VO_2	oxygen consumption
X_p	non-elastic portion of the contractile element equal to *halfSL* - h_p
X_w	non-elastic portion of the contractile element equal to *halfSL* - h_w
Y_b	kinetic reaction constant for the binding Ca^{2+} step
Y_p	Ca^{2+} kinetic reaction constant
Y_r	Ca^{2+} kinetic reaction constant
Y_v	parameter describing the effect of h_w on g
Z_a	kinetic reaction constant for the CB detaching step
Z_b	kinetics reaction constant for the binding Ca^{2+} step
Z_p	Ca^{2+} kinetic reaction constant
Z_r	Ca^{2+} kinetic reaction constant

Chapter 1: Introduction

1.1 Research background and purpose of the study

Cardiovascular diseases are responsible for the deaths in human for several decades. Heart failure which caused from the ineffective contraction is the majority among those cardiovascular diseases. The understanding of cardiovascular system under physiological conditions has been progressed, nevertheless, it is not fully understood.

Information technogy allows us to understand the complex of biological mechanisms of the cardiovascular system. Cardiac muscle cells or cardiomyocytes play an important role in the cardiovascular system. Cardiomyocyte function, in particularly, crossbridge work is driven by the energy from adenosine 5′-triphosphate (ATP). This tight coupling between energy production and consumption is essential to maintain the normal activity.

We have well known that the energy is mainly utilized by the interaction of crossbridge (CB) in cardiomyocytes. Since the mechanisms of CB are not clearly understood, the development of CB model could provide the valuable tool to comprehend those reaction or energy consumption. The CB model which well concerns the key of biological functions and mechanisms could be implemented into multi-scale model of cardiovascular system for a better understanding of those energy consumptions.

On the other hand, the cardiomyocytes have a high mitochondrial density to supply the energy in form of ATP resisting the fatigue. The mutations in mitochondrial DNA sequences cause the malfunction of ATP production leading to cardiomyopathies. The early-stage detection of those mutations could be an advantage for health evaluation.

The objectives of this study were following;

1) to develop the new CB model based on the molecular mechanisms of ATP-hydrolysis by S1 segment of myosin with the biophysical contraction model and implemented in the multi-scale model of cardiovascular system

2) to improve the specific techniques for diagnosing the mutations in cytochrome *b* gene sequence of mitochondrial DNA that leading to cardiomyopathies

To success those objectives, this dissertation was divided into two parts; 1) the energy consumption by CB mechanisms using computational modeling and 2) the energy production focused on the detection of insufficient function from mutations in cytochrome *b* gene sequence of mitochondrial DNA.

1.2 Cardiomyocytes; energy production and consumption

The structure of cardiomyocyte is well known as described in Figure 1-1. Unlike the other cells, the membrane of cardiomyocyte contains specific proteins which connect to nearby cardiomyocytes as the mechanical and electrical partners. Cardiomyocytes in mammals contain myofibrils which involved with the muscle contraction. They pump the blood into vessels of circulatory system via the excitation-contraction coupling. The cardiomyocyte of human is a roughly cylindrical-shape cell and some cardiomyocytes are branched. The size is 10-20 μm × 50-100 μm (wide × long). The intercalated disc is adjacent at end-to-end between two myocytes including; gap junction (electrical conduction), desmosome (mechanical strength).

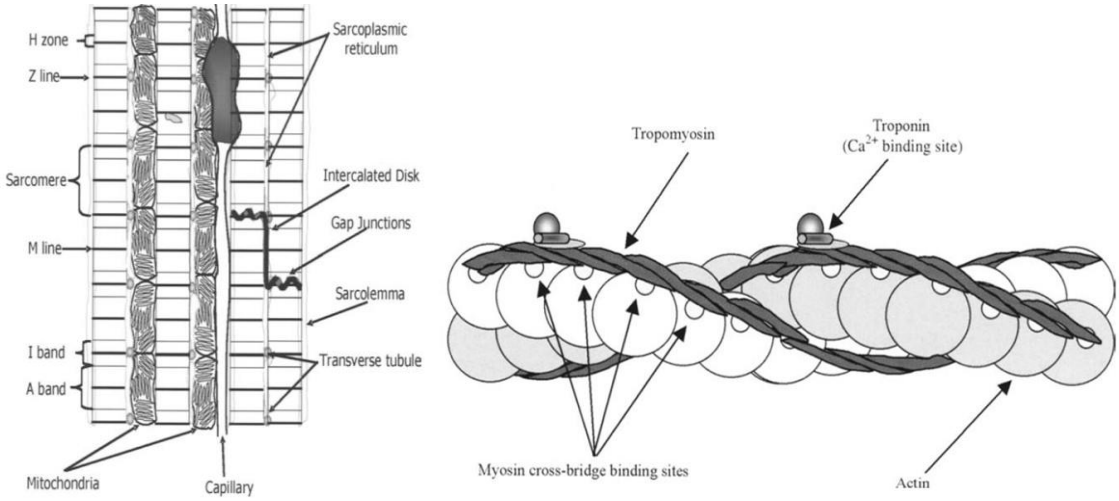

Figure 1-1 The structure of cardiomyocyte. *Left*; The structure of cardiac cell including the sarcomeric organization of fundamental contractile proteins and other key elements. The sarcomere of human heart is approximately 2.0 μm in length at rest. *Right*; Calcium regulation of contraction on thin filament. Calcium binding to troponin induces tropomyosin movement, allowing the development of force.

[Z line = the border line on each end located by a protein matrix, A band = the region of the sarcomere in which the myosin filaments reside, I band = the area between A bands of adjacent sarcomeres]

Source Barnett 2009

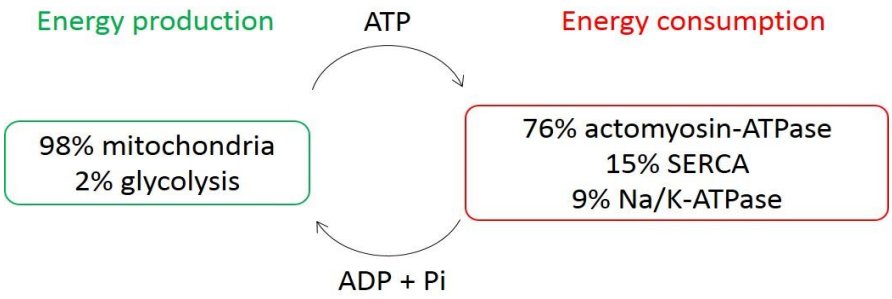

Figure 1-2 Cardiac muscle metabolisms; the main activity of energy production from mitochondria and consumption from actomyosin-ATPases (Schramm et al. 1994).

[SERCA = sarcoplasmic reticulum Ca^{2+}-ATPase]

Energy production and consumption mechanisms play an important role in vital mechanisms of cardiomyocytes (Figure 1-2). However, the explicit details that could explain either energy production and consumption at molecular or sub-molecular level are not clearly understood. Here, we focused on 1) the actomyosin ATPase that mainly consume energy, 2) mitochondrial DNA that produce energy for the work of cardiomyocytes. For energy production part, our interest was the integrative method for detection of the mutations in cytochrome *b* gene sequence of mitochondrial DNA.

1.2.1 Mitochondria and energy production

Mitochondria mainly produces the energy for cell activities via respiratory chain or electron transport chain. The electron transport system is embedded in the inner membrane of mitochondria. Two energy carriers; 1) nicotine adenine dinucleotide (NAD) and 2) flavin adenine dinucleotide (FAD), carry the energy to complex I and complex II, respectively. Genes in mitochondria provide the necessary proteins involved with oxidative phosphorylation. The mitochondrial genome sized about 16,500 base pairs includes 37 mitochondrial DNA-encoded genes; 13 coding genes, 2 ribosomal RNAs (12S and 16S), and 22 transfer RNAs (Figure 1-3). Five protein complexes are embedded at the inner layer of mitochondrial membrane.

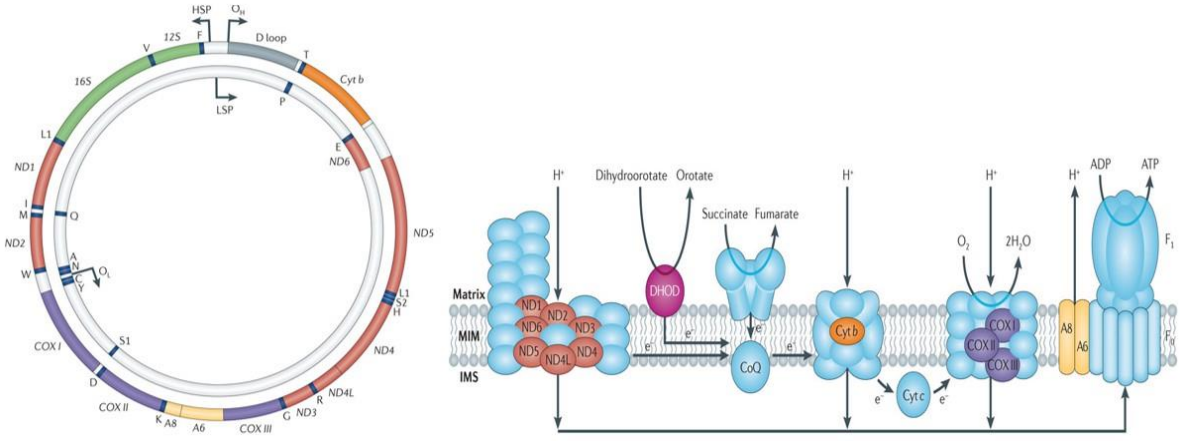

Figure 1-3 *Left*; Human mitochondrial genome, *Right*; Oxidative phosphorylation; electron transport chain. [The composition of mitochondrial DNA and 37 encoded genes including; complex I 'NADH-coenzyme Q reductase complex' (*ND1*, *ND2*, *ND3*, *ND4*, *ND4L*, *ND5*, and *ND6*) [*ND = NADH dehydrogenase*], complex II 'succinate dehydrogenase complex', complex III 'cytochrome bc_1 complex' (cytochrome *b*), complex IV 'cytochrome oxidase complex' (*COXI*, *COXII*, and *COXIII*) [*COX* = cytochrome *c* oxidase], complex V (*A6*, and *A8*), [*A = ATP synthase*], two ribosome RNAs (12S and 16S), twenty-two transfer RNAs (*Left*; one-letter code [A Alanine, R Arginine, N Asparagine, D Aspartic acid, C Cysteine, E Glutamic acid, Q Glutamine, G Glycine, H Histidine, I Isoleucine, L Leucine, K Lysine, M Methionine, F Phenylalanine, P Proline, S Serine, T Threonine, W Tryptophan, Y Tyrosine, V Valine], origin of replication of the heavy chain (O_H) and light chain (O_L), and the promoters of transcription of the heavy strand (HSP) and light strand (LSP)]

Source Schon et al. 2012

1.2.2 Cardiac muscle contraction and energy consumption

Cardiomyocytes mainly utilize the energy by muscle contraction activity (Suga 1990, Schramm et al. 1994). The contraction results from a sliding of CB involved with two major filaments; actin and myosin. The CB continuously moves by attachment and detachment steps driven by the hydrolyzing of ATP catalyzed by actomyosin-ATPase enzyme. These mechanisms are the major component of ATP consumption in the cardiac muscle (Suga 1990). More than a half-century, the study of CB mechanisms based on structural, biochemical, and physiological aspects have been revealed. However, the interaction of CB coupling to ATP hydrolysis is still unclear. As minimum requirements, the new model should capture as the following essential aspects of key CB cycle tightly bound with ATP-hydrolysis cycle as Figure 1-4.

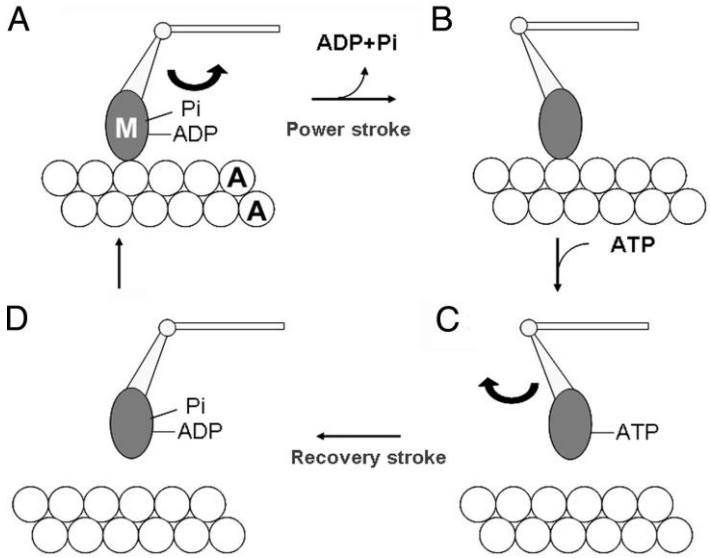

Figure 1-4 The illustration of the crossbridge (CB) cycle between myosin (M) and actin (A) in the cardiac myocytes.

Phase A; The tropomyosin is dislocated by the binding of Ca^{2+} to troponin during the cytosol Ca^{2+} transient (Ford 1991). The myosin head with ADP + Pi (*M ADP Pi*) attaches to actin myofilament, forming weakly bound state of CB. During phase A to phase B, the dissociation of inorganic Phosphate (Pi) from the S1 segment is tightly coupled with the force generation of the CB, resulting in the 'power stroke / filament sliding'. Myosin head pivots and bends as it pulls on the actin filament and then ADP is released.

Phase B; At the end of power stroke 'post-power stroke configuration', CB forms the rigor conformation.

Phase C; The replacement of ADP by a new ATP accompanied with relaxation of rigor conformation occurs even in the absence of actin and Ca^{2+} (Sugi et al. 2008, Minoda et al. 2011) and CB detaches.

Phase D; ATP is hydrolyzed (*M ATP* → *M ADP Pi*) associated with a structural change with a swing of the myosin lever arm. ADP and Pi remain bound to the active site of myosin head (Lymn & Taylor 1971, Sugi et al. 2008).

Source: Sugi et al. 2008

The formation of CB interaction could be summarized into six states: 1) M ADP Pi → 2) AM ADP Pi → 3) AM ADP → 4) AM → 5) AM ATP → 6) M ATP. This assumption is described as the minimum requirements as the Figure 1-5 (Geeves et al. 2005) and the wide studies (Lombardi & Piazzesi 1990, Dantzig et al. 1992, Ebus et al. 1994, Piazzesi & Lombardi 1996, Månsson 2010, Bickham et al. 2011, Månsson et al. 2015).

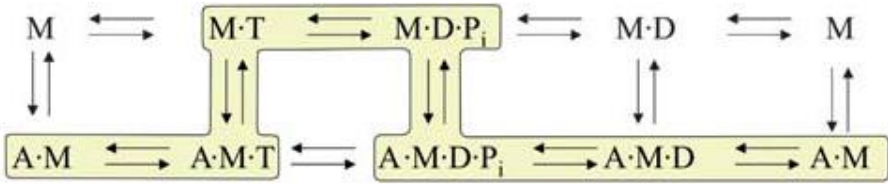

Figure 1-5 The minimal description of the interaction between action and myosin ATPase.
[M = myosin ATPase, A = actin, T = ATP, D = ADP, and P_i = inorganic phosphate]
Source: Geeves et al. 2005

1.3 Cardiac muscle contraction model

The cardiac muscle contraction is described by the relationship between length and tension. It is classified as isometric contraction (generating tension without changing length) and isotonic contraction (muscle length changes but tension remains the same). However, the definite understanding of CB mechanism is still unclear. The various whole cell models have been developed to explain the CB mechanisms by using mathematical model describes different aspects of mechanical activity of muscle underlying the physiological regulation of cardiac contraction.

1.3.1 Theory of muscle contraction and modeling

Huxley's CB dynamics is widely used in understanding the muscle work and subunits of muscle (Huxley 1957). Huxley developed the basic model to explain the force generation follows the CB attachment step with the different conformational state. The first proposed model of Huxley was as follows; 1) there is an elastic element in the CB, 2) the CB generates force immediately upon formation, 3) there is a limited rate constant for CB formation, and 4) the rate constant of CB dissociation increases if the elastic force counteracts shortening. The construction of model based on the mechanochemical cycle of CB requires partial differential equations (Huxley1957).

A variety of myofilament model with the Huxley-based contraction model implemented the Ca^{2+} transient function to act as the biophysiological function (Lombardi & Piazzesi 1990, de Tombe & Ter Keurs 1991, Landesberg & Sideman 1994, Piazzesi & Lombardi 1995, Negroni & Lascano 1996, 1999, 2008, Rice et al. 2003, Razumova et al. 1999, Negroni et al. 2015). Negroni & Lascano model 'NL model' (Negroni & Lascano 1996 & 2008) which assumed a relatively simple equivalent CB (eCB), whose distortion is represented with a linear spring and its sliding along the actin filament is calculated by assuming a movable viscosity head. These approximations seem to be roughly in common with the Rice model (2008). NL model has also been used in developing various types of ventricular models (Matsuoka

et al. 2003, 2004, Okada et al. 2005, Shim et al. 2007, 2008, Asakura et al. 2014, Himeno et al. 2015). NL model well describes Hill coefficient (close to 4) and successfully reconstructs most of the key mechanical events of the cardiac muscle so far described in biophysical studies using the experiment data; the step changes in length (Huxley & Simmons 1971, Huxley 1974, Ford et al. 1977), steady force-length-[Ca^{2+}] relations (Kentish et al. 1986), the time course of [Ca^{2+}] following step changes in length related to troponin C (Lab et al. 1984), the frequency dependence of the stiffness modulus (Shibata et al. 1987), force-velocity relation (de Tombe & ter Keurs 1991), the velocity of force re-development following length pulses (Peterson et al. 1991), force-length relations for isometric twitches (Kentish et al. 1986, de Tombe & ter Keurs 1991), time course of force following quick release (Nwasokwa et al. 1984), and time course of active state (Chiu et al. 1987, Ford 1991). NL model represents a myocyte as a series arrangement of units (Figure 1-6).

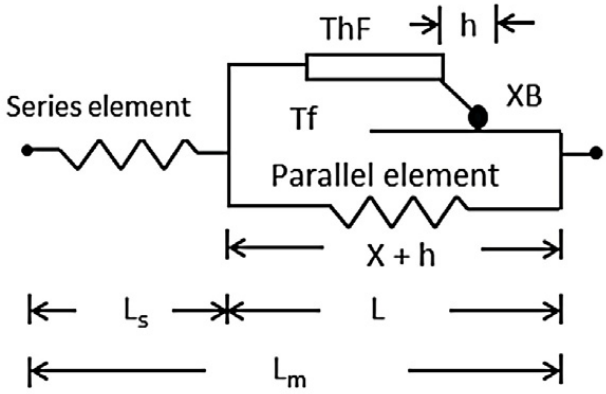

Figure 1-**6** Constitutive muscle unit; defined by half sarcomere length (*L*) and cross-sectional area. In this Figure, *L* is composed of thick filament (*ThF*) and thin filament (*Tf*) in parallel with an internal elastic element. *ThF* and *Tf* can slide past each other and the overlap area where the equivalent crossbridge (*XB*) can attach to *Tf*.

[h = crossbridge elongation, L_s = length of series elastic element, L_m = total muscle length]

Source: Negroni et al. 2015

Negroni & Lascano (1996) established four-state system of CB dynamics and intracellular Ca^{2+} kinetics for cardiac muscle. The model well described the relation of mechanical behavior with sarcomere dynamics and Ca^{2+} kinetics. Their assumptions are 1) force is developed by the attached CB and the number of attached CB depends on sarcomere length, 2) attached CB develops force according to elongation of their elastic structure, 3) at a steady sarcomere length, there is a unique CB elongation and, during changes in sarcomere length, the concurrent change in CB length is re-adjusted to the steady state value by the detachment and re-attachment in the new position along the thin myofilament, and 4) the increased CB detachment during changes in sarcomere length depends on the rate of re-adjustment of CB elongation. The model was modified to six-state contraction model (Negroni & Lascano 2008) by including weak and power attached CBs (Figure 1-7).

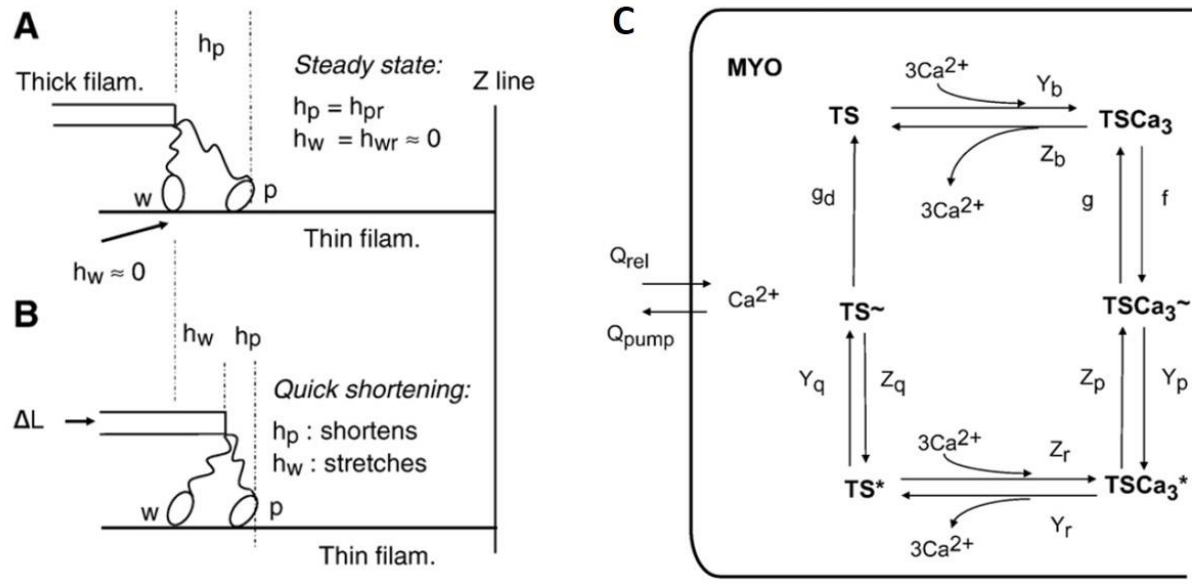

Figure 1-7 Equivalent weak (w) and power (p) CB state at steady state (panel A) and at quick shortening (panel B). Panel A; $h_w = h_{wr}$ is close to zero and $h_p = h_{pr}$ is greater than zero. Panel B; after a length step, the reduction in half sarcomere length produces an increase in h_w and a decrease in h_p. Panel C; Six states of troponin system (TS) and Ca^{2+} flow from sarcoplasmic reticulum. Q_{rel} and Q_{pump} represent Ca^{2+} flow in and out acting on the myoplasm (MYO), respectively.

[h_w = mean elongation of attached CBs in the weak state, h_p = mean elongation of attached CBs in the power work state, h_{wr} = steady elongation of attached CBs in the weak state, h_{pr} = steady elongation of attached CBs in the power work state, ΔL = the changes in half sarcomere length, f = attachment step, g & g_d = detachment step, Y = forward step, Z = reverse step, TS = free TS, $TSCa_3$ = Ca^{2+} bound to TS without attached CBs, $TSCa_3$~ = Ca^{2+} bound to TS with attached CBs in the weak state, $TSCa_3$* = Ca^{2+} bound to TS with attached CBs in the power state, TS* = TS without Ca^{2+} with attached CBs in the power state, TS~ = TS without Ca^{2+} with attached CBs in the weak state]

Source: Negroni & Lascano 2008

1.3.2 Mechanoenergetics of actomyosin interaction

On the other hand, the myofilament model which is based on the Huxley hypothesis of independent CB behavior adopts the hypothetical Gibb's free energy profile to describe the state transition of CB. The additional biochemical and mechanical states have been introduced and some models implemented the intermolecular cooperativity (Duke 1999, Tanner et al. 2007, Smith et al. 2008, Smith & Mijailovich 2008). The 11 predominant reaction states of actomyosin (AM) ATPase were identified in skeletal muscle proposed by Månsson et al. (2015). Each transitional state based on the details of the biochemical and structural states of the CB cycle (Figure 1-8).

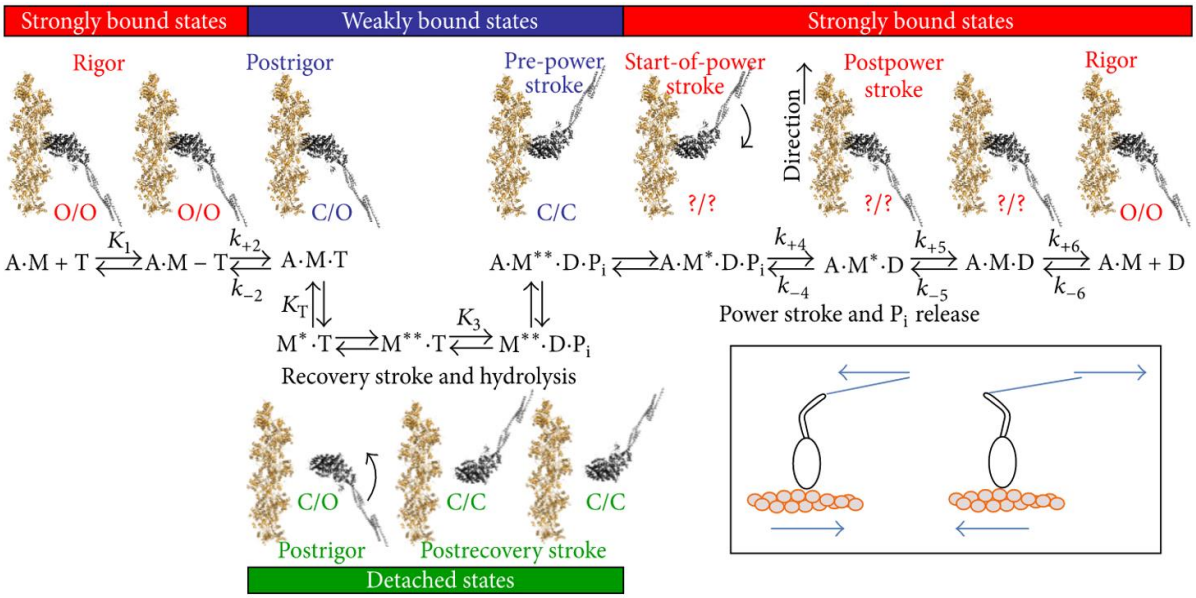

Figure 1-8 Predominant biochemical and structural states of actomyosin ATPase cycle. Orange and black cartoons indicate the action and myosin, respectively. The open (O) or close (C) conformation of the active site elements is indicated by switch 1 and 2. Switch 1 is designated as the first. The power stroke corresponds to switch 2 closed-to-open transition while the myosin motor domain is bound to actin.
Inset: Schematics illustration of tension in lever arm; *left* = shortening, *right* = resist shortening
[A = actin, M = myosin, T = ATP, D = ADP, P = P_i or inorganic phosphate, *k* or *K*= rate functions]
Source: Månsson et al. 2015

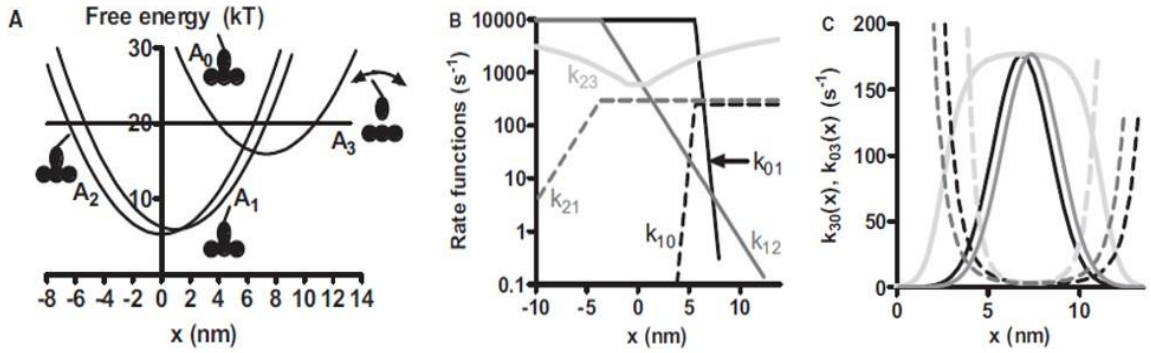

Figure 1-9 Free-energy profiles and rate function. Panel A; Free energy at detached state (A_3) is 20 kT (Barclay 1998, Sleep et al. 2005) used for all values of *x*. The bent double arrow indicates the lever arm is disclosed in this state. The illustration of the equilibrium lever arm positions for the different states is given. A_0, A_1, A_2, and A_3 indicate AMDP, AM*D, lumped state of AMD, AM & AMT, and lumped state of MT & MDP, respectively. Panel B; Rate functions for transition between attached states ($k_{01}(x)$, $k_{10}(x)$, $k_{12}(x)$, $k_{21}(x)$) and detachment rate function ($k_{23}(x)$). Panel C; attachment ($k_{30}(x)$) and detachment rate functions ($k_{03}(x)$) are illustrated in full and dash line, respectively. Black line refers to standard simulations, dark and light gray refer to some specific simulations).
Source Månsson 2010

Månsson (2010) lumped 11 predominant states to four-state biochemical model which well represented four essential steps of the ATP-hydrolysis; 1) AMDP, 2) AM*D, 3) AMD, AM, AMT are lumped, 4) MT and MDP are lumped. This simpler model captures the most essential aspects of key phenomena and can be identified by the experimental results. Additionally, the rate functions are related to the relative distance between myosin head and a nearest actin binding site for each CB (Figure 1-9). The model assumed that there is a uniform distribution of myosin heads with respect to the distance to the nearest actin binding site. It is well-motivated in statistical models of essential consideration including; 1) the mismatch between the myosin and actin filament periodicities which described by Smith et al. (2008), 2) the misalignment between neighboring myofilaments over the fiber cross-section (Edman & Reggiani 1987), and 3) the non-uniform in lengths of sarcomere along the length of muscle fiber (Edman & Reggiani 1984).

1.3.3 Myocardial energetics of ventricular cell model

Two apparently fundamentally different modes of the energetics of muscle contraction investigation have dominated the study of cardiac energetics. 1) Gibbs group (Ricchiuti & Gibbs 1965, Gibbs 1967, Gibbs et al. 1967) measured the heat production and work performance of one-dimensional isolated papillary muscle using the flat-bed thermopile described by linear relationship of heat-force, and 2) Suga group (Khalafbeigui et al. 1979, Suga 1979) measured the oxygen consumption (VO_2) of whole hearts performing pressure-volume work described the total mechanical energy generated in a cardiac contraction by pressure-volume area (*PVA*). Han et al. (2012), however, summarized that the fundamental difference between Suga's phenological isoefficiency and Gibbs's load-dependent efficiency cannot be reconciled.

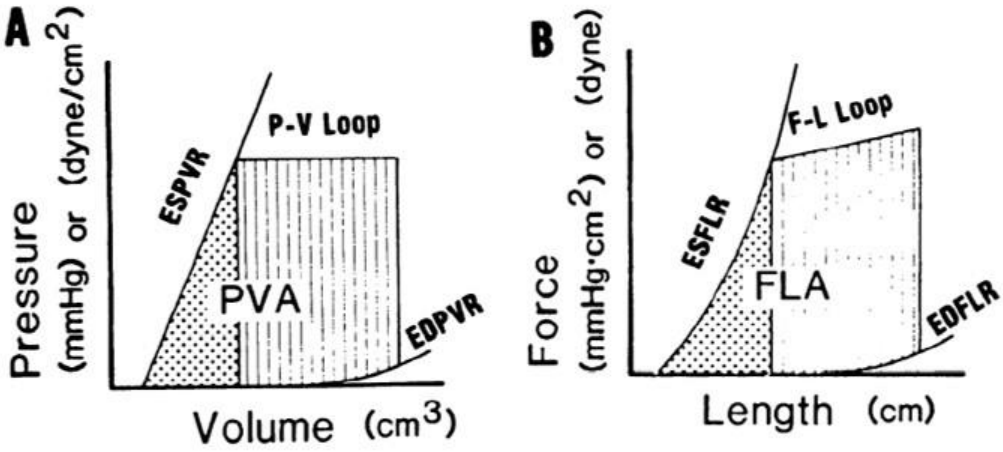

Figure 1-10 The comparison pressure-volume area (*PVA*) and force-length area (*FLA*). Panel A; *PVA* is composed of end-systolic pressure-volume relation (*ESPVR*), end-diastolic pressure-volume relation (*EDPVR*), and pressure-volume loop (*PV* loop). Panel B; *FLA* is related with end-systolic force-length relationship (*ESFLR*), the end-diastolic force-length relation (*EDFLR*), and force-length (*F-L* loop).
Source: Taylor et al. 1993

The force-length area (*FLA*) is analogous to *PVA*, and both are linearly correlated with cardiac energy consumption reported in animal experiments (Hisano & Cooper 1987, Suga 1990) (Figure 1-10). *PVA* describes the mechanisms of left ventricular in four phases 1) the filling phase, 2) the isovolumic ventricular contraction, 3) the ventricular ejection, and 4) the isovolumic ventricular relaxation. These four phases are commonly plotted as the relationship between pressure and volume or 'pressure-volume loop (*PV* loop)'. Each corner represents a valve action, each side a phase.

1.4 References

Asakura K, Cha CY, Yamaoka H, Horikawa Y, Memida H, Powell T, Amano A, Noma A (2014) EAD and DAD mechanisms analyzed by developing a new human ventricular cell model. Prog Biophys Mol Biol 116:11-24

Barclay CJ (1998) Estimation of cross-bridge stiffness from maximum thermodynamic efficiency. J Muscle Res Cell Motil 19:855-864

Barnett VA (2009) Cardiac myocytes. *In* Handbook of cardiac anatomy, physiology, and devices, Iaizzo PA (ed), Humana Press Inc., Totowa, NJ, pp 113-121

Bickham DC, West TG, Webb MR, Woledge RC, Curtin NA, Ferenczi MA (2011) Millisecond-scale biochemical response to change in strain. Biophys J 101:2445-2454

Chiu YC, Ballou EW, Ford LE (1987) Force, velocity and power changes during normal and potentiated contractions of cat papillary muscle. Circ Res 60:446-458

Dantzig JA, Goldman YE, Miller NC, Lacktis J, Homsher E (1992) Reversal of the cross-bridge force-generating transition by photogeneration of phosphate in rabbit psoas muscle fibres. J Physiol 451:247-278

de Tombe PP, ter Keurs HE (1991) Sarcomere dynamics in cat cardiac trabeculae. Circ Res 68:588-596

Duke TA (1999) Molecular model of muscle contraction. Proc Natl Acad Sci USA 96:2770-2775

Ebus JP, Stienen GJ, Elzinga G (1994) Influence of phosphate and pH on myofibrillar ATPase activity and force in skinned cardiac trabeculae from rat. J Physiol 476:501-516

Edman KAP, Reggiani C (1984) Redistribution of sarcomere length during isometric contraction of frog muscle fibres and its relation to tension creep. J Physiol 351:169-198

Edman KAP, Reggiani C (1987) The sarcomere length-tension relation determined in short segments of intact muscle fibres of the frog. J Physiol 385:709-732

Ford LE (1991) Mechanical manifestations of activation in cardiac muscle. Circ Res 68:621-637

Ford LE, Huxley AF, Simmons RM (1977) Tension responses to sudden length change in stimulated frog muscle fibres near slack length. J Physiol 269:441-515

Geeves MA, Fedorov R, Manstein DJ (2005) Molecular mechanism of actomyosin-based motility. Cell Mol Life Sci 62:1462-1477

Gibbs CL (1967) Role of catecholamines in heat production in the myocardium. Circ Res 21(suppl.3): 223-230

Gibbs CL, Chapman JB (1985) Cardiac mechanics and energetics: chemomechanical transduction in cardiac muscle. Am. J Physiol Heart Circ Physiol 249:H199-H206

Gibbs CL, Mommaerts WFHM, Ricchiuti NV (1967) Energetics of cardiac contractions. J Physiol 191:25-46

Han JC, Taberner AJ, Tran K, Goo S, Nickerson DP, Nash MP, Nielsen PMF, Crampin EJ, Loiselle DS (2012) Comparison of Gibbs and Suga formations of cardiac energetics: the demise of "isoefficiency". J Appl Physiol 113:996-1003

Himeno Y, Asakura K, Cha CY, Memida H, Powell T, Amano A, Noma A (2015) A human ventricular myocyte model with a refined representation of excitation-contraction coupling. Biophys J 109:415-427

Hisano R, Cooper G (1987) Correlation of force-length area with oxygen consumption in ferret papillary muscle. Circ Res 61:318-328

Huxley AF (1957) Muscle structure and theories of contraction. Prog Biophys Biophys Chem 7:255-318

Huxley AF (1974) Muscle contraction. J Physiol 243:1-43

Huxley AF, Simmons RM (1971) Proposed mechanism of force generation in striated muscle. Nature 233:533-538

Kentish JC, ter Keurs HEDJ, Ricciardi L, Bucx JJJ, Noble MIM (1986) Comparison between the sarcomere length-force relations of intact and skinned trabeculae from rat right ventricle. Circ Res 58:755-768

Khalafbeigui F, Suga H, Sagawa K (1979) Left ventricular systolic pressure-volume area correlates with oxygen consumption. Am J Physiol Heart Circ Physiol 237:H566-H569

Lab MJ, Allen DG, Orchard CH (1984) The effects of shortening on myoplasmic calcium concentration and on the action potential in mammalian ventricular muscle. Circ Res 55:825-829

Landesberg A, Sideman S (1994) Mechanical regulation of cardiac muscle by coupling calcium kinetics with cross-bridge cycling: a dynamic model. Am J Physiol Heart Circ Physiol 267:H779-H795

Lombardi V, Piazzesi G (1990) The contractile response during steady lengthening of stimulated frog muscle fibres. J Physiol 431:141-171

Lymn RW, Taylor EW (1971) Mechanism of adenosine triphosphate hydrolysis by actomyosin. Biochemistry 10:4617-4624

Månsson A (2010) Actomyosin-ADP states, interhead cooperativity, and the force-velocity relation of skeletal muscle. Biophys J 98:1237-1246

Månsson A, Rassier D, Tsiavaliaris G (2015) Poorly understood aspects of striated muscle contraction. Biomed Res Int. doi:10.1155/2015/245154

Matsuoka S, Sarai N, Jo H, Noma A (2004) Simulation of ATP metabolism in cardiac excitation–contraction coupling. Prog Biophys Mol Biol 85:279-299

Matsuoka S, Sarai N, Kuratomi S, Ono K, Noma A (2003) Role of individual ionic current systems in ventricular cells hypothesized by a model study. Jpn J Physiol 53:105-123

Minoda H, Okabe T, Inayoshi Y, Miyakawa T, Miyauchi Y, Tanokura M, Katayama E, Wakabayashi T, Akimoto T, Sugi H (2011) Electron microscopic evidence for the myosin head lever arm mechanism in hydrated myosin filaments using the gas environment chamber. Biochem Biophys Res Commun 405:651-656

Negroni JA, Lascano EC (1996) A cardiac muscle model relating sarcomere dynamics to calcium kinetics. J Mol Cell Cardiol 28:915-929

Negroni JA, Lascano EC (2008) Simulation of steady state and transient cardiac muscle response experiments with a Huxley-based contraction model. J Mol Cell Cardiol 45:300-312

Negroni JA, Morotti S, Lascano EC, Gomes AV, Grandi E, Puglisi JL, Bers DM (2015) β-adrenergic effects on cardiac myofilaments and contraction in an integrated rabbit ventricular myocyte model. J Mol Cell Cardiol 81:162-175

Nwasokwa O, Sagawa K, Suga H (1984) Short-term memory in the in situ canine myocardium. Am J Physiol Heart Circ Physiol 247:H8-H16

Okada JI, Sugiura S, Nishimura S, Hisada T (2005) Three-dimensional simulation of calcium waves and contraction in cardiomyocytes using the finite element method. Am J Physiol Cell Physiol 288:C510-C522

Peterson JN, Hunter WC, Berman MR (1991) Estimated time course of Ca^{2+} bound to troponin C during relaxation in isolated cardiac muscle. Am J Physiol Heart Circ Physiol 260:H1013-H1024

Piazzesi G, Lombardi V (1995) A cross-bridge model that is able to explain mechanical and energetic properties of shortening muscle. Biophys J 68:1966-1979

Piazzesi G, Lombardi V (1996) Simulation of the rapid regeneration of the actin-myosin working stroke with a tight coupling model of muscle contraction. J Muscle Cell Motil 17:45-53

Razumova MV, Bukatina AE, Campbell KB (1999) Stiffness-distortion sarcomere model for muscle simulation. J Appl Physiol 87:1861-1876

Ricchiuti NV, Gibbs CL (1965) Heat production in a cardiac contraction. Nature 208:897-898

Rice JJ, Stolovitzky G, Tu Y, de Tombe PP (2003) Ising model of cardiac thin filament activation with nearest-neighbor cooperative interactions. Biophys J 84:897-909

Rice JJ, Wang F, Bers DM, de Tombe PP (2008) Approximate model of cooperative activation and crossbridge cycling in cardiac muscle using ordinary differential equations. Biophys J 95:2368-2390

Schramm M, Klieber HG, Daut J (1994) The energy expenditure of actomyosin-ATPase, Ca^{2+}-ATPase and Na^{+}, K^{+}-ATPase in guinea-pig cardiac ventricular muscle. J Physiol 481:647-662

Shibata T, Hunter WC, Yang A, Sagawa K (1987) Dynamic stiffness measured in central segment of excised rabbit papillary muscles during barium contracture. Circ Res 60:756-769

Shim EB, Amano A, Takahata T, Shimayoshi T, Noma A (2007) The cross-bridge dynamics during ventricular contraction predicted by coupling the cardiac cell model with a circulation model. J Physiol Sci 57:275-285

Shim EB, Jun HM, Leem CH, Matusuoka S, Noma A (2008) A new integrated method for analyzing heart mechanics using a cell-hemodynamics-autonomic nerve control coupled model of the cardiovascular system. Prog Biophys Mol Biol 96:44-59

SiMauro S, Hirano M (2012) Human mitochondrial DNA: roles of inherited and somatic mutations. Nat Rev Genet 13:878-890

Sleep J, Irving M, Burton K (2005) The ATP hydrolysis and phosphate release steps control the time course of force development in rabbit skeletal muscle. J Physiol 563:671-687

Smith DA Geeves MA, Sleep J, Mijailovich SM (2008) Towards a unified theory of muscle contraction. I: Foundations. Ann Biomed Eng 36:1624-1640

Smith DA, Mijailovich (2008) Toward a unified theory of muscle contraction. II: Prediction with the mean-field approximation. Ann Biomed Eng 36:1353-1371

Suga H (1979) Total mechanical energy of a ventricle model and cardiac oxygen consumption. AM J Physiol Heart Circ Physiol 236:H498-H505

Suga H (1990) Ventricular energetics. Physiol Rev 70:247-277

Sugi H, Minoda H, Inayoshi Y, Yumoto F, Miyakawa T, Miyauchi Y, Tanokura M, Akimoto T, Kobayashi T, Chaen S, Sugiura S (2008) Direct demonstration of the cross-bridge recovery stroke in muscle thick filaments in aqueous solution by using the hydration chamber. Proc Natl Acad Sci USA 105:17396-17401

Tanner BC, Daniel TL, Regnier M (2007) Sarcomere lattice geometry influences cooperative myosin binding in muscle. PloS Comput Biol 3:e115

Taylor TW, Goto Y, Suga H (1993) Variable cross-bridge cycling-ATP coupling accounts for cardiac mechanoenergetics. Am J Physiol Heart Circ Physiol 264:H994-H1004

Wallace DC (1999) Mitochondrial diseases in man and mouse. Science 283:1482-1488

Chapter 2: New mathematical model of cardiac contraction model

Here, we developed a new contraction model 'Hybrid model' which combined the reaction steps of ATP-hydrolysis by S1 segment of 'Månsson model' with Huxley-type contraction model developed by Negroni and Lascano (2008) 'NL model' which assumes an equivalent crossbridge (eCB) as a representation of average behavior of all crossbridge (CB). The model concerned the dominant characteristic of both models (Table 2-1).

Table 2-1 The characteristic of NL model and Månsson model.

NL model	Månsson model
Cardiac cell	Skeletal muscle cell
Biophysiological mode	In vitro experiment
Rate of elongation change (*dh/dt*)	Function of the distance (*x*)
Ca^{2+} application with time course	Steady state during tetanus
Ca^{2+} dependency	Ca^{2+} fixed
Isometric and isotonic contraction	Isometric contraction (mainly)
Detachment rate depends on weak states (h_w)	Detachment rate depends on power state (h_p)
-	ATP consumption

Hybrid model mainly adopted from NL model which is characterized by the introduction of the eCB which largely facilitates the calculation of the developed force of contraction in the continuous manner. Moreover, NL model successfully reconstructs the most of key mechanical events of the cardiac muscle so far described in the extensive biophysical studies, such as the time course of developed tension evoked by the membrane excitation, as well as those evoked by applying step changes in the isometric and isotonic contraction model at various Ca^{2+} concentration. The mechano-chemical contraction model has been proved for its efficiency when integrated into a variety of cardiac cell model (Cenci et al. 2010, Lascano et al. 2013, Asakura et al. 2014, Himeno et al. 2015). The simplification was achieved not really developing a specific algorithm for averaging the behavior of all CBs, the magnitude as well as the time course of reconstructed crossbridge force (F_b) well agrees with the experimental findings. This eCB assumption was adopted in the present model as in the original NL model.

On the other hand, the details of the rate constant defined in the Månsson model should be found in Chapter 1.3.2 and more in the original publications (Månsson 2010, Månsson et al. 2015) based on the free energy assumption. However, Månsson model is still difficult to use in the whole cell model of excitation-contraction coupling, because the models concern with CB kinetics in the continuous presence of a steady Ca^{2+} concentration during tetanus contraction of skeletal muscle. Moreover, the profile of free energy of various states of CB is still largely variable between different models proposed (Lombardi & Piazzesi 1990, Piazzasi & Lombardi 1995, Månsson 2010) especially when the critical parameter of sliding

velocity of myofilament is included in the kinetics. For those reasons, the original rate constants, which were theoretically elaborated in Månsson model were simplified in reference to the kinetics of eCB. Thus, in the present study, we readjusted the rate of state transitions to get a new contraction model, which conforms to experiment findings in both the kinetics measurements of the developed tension and the ATP consumption measured in macroscopic levels.

2.1 New eight-state transition model 'Hybrid model'

Our eight-state transition model, the main parameters are adopted from Negroni and Lascano (2008) and Negroni et al. (2015). Some model parameters are adjusted to reproduce the experimental data. Moreover, each state is postulated using the biological state that involved the ATP utilization of CB (Lombardi & Piazzesi 1990, Piazzesi & Lombardi, 1995, Månsson 2010). The new model performs the satisfactory results for the calculation of ATP usage by cardiac muscle contraction (Figure 2-1) and each state described in Table 2-2.

Table 2-2 Eight-state transition model

State	Structure	Description
AM_T	Post-rigor	ATP binds to S1 segment of myosin in the place of ADP
M_{DP} (M_T)	Recovery stroke	The hydrolysis of ATP to ADP and Pi changes conformation of myosin lever arm from rigor to recovery stroke
cM_{DP}	Post-recovery stroke	Ca^{2+} molecules rapidly bind to troponin-tropomyosin unit and tropomyosin opens
cAM_{DPw}	Pre-power stroke	S1 segment attachment initials the weak conformation then establishes to power crossbridge conformation
cAM_{Ds}	Post-power stroke	Myosin head structure changes from rest to rigor conformation
cAM_T	Post-rigor	ATP binds to S1 segment in the place of ADP and relaxing the rigor state through the temporal dissociation of crossbridge
cM_{DP} (cM_T)	Post-recovery stroke	The hydrolysis of ATP to ADP and Pi changes conformation of myosin lever arm from rigor to recovery stroke
AM_{Ds}	Rigor	Ca^{2+} molecules release from troponin-tropomyosin unit (tropomyosin closes) and crossbridge forms rigor state

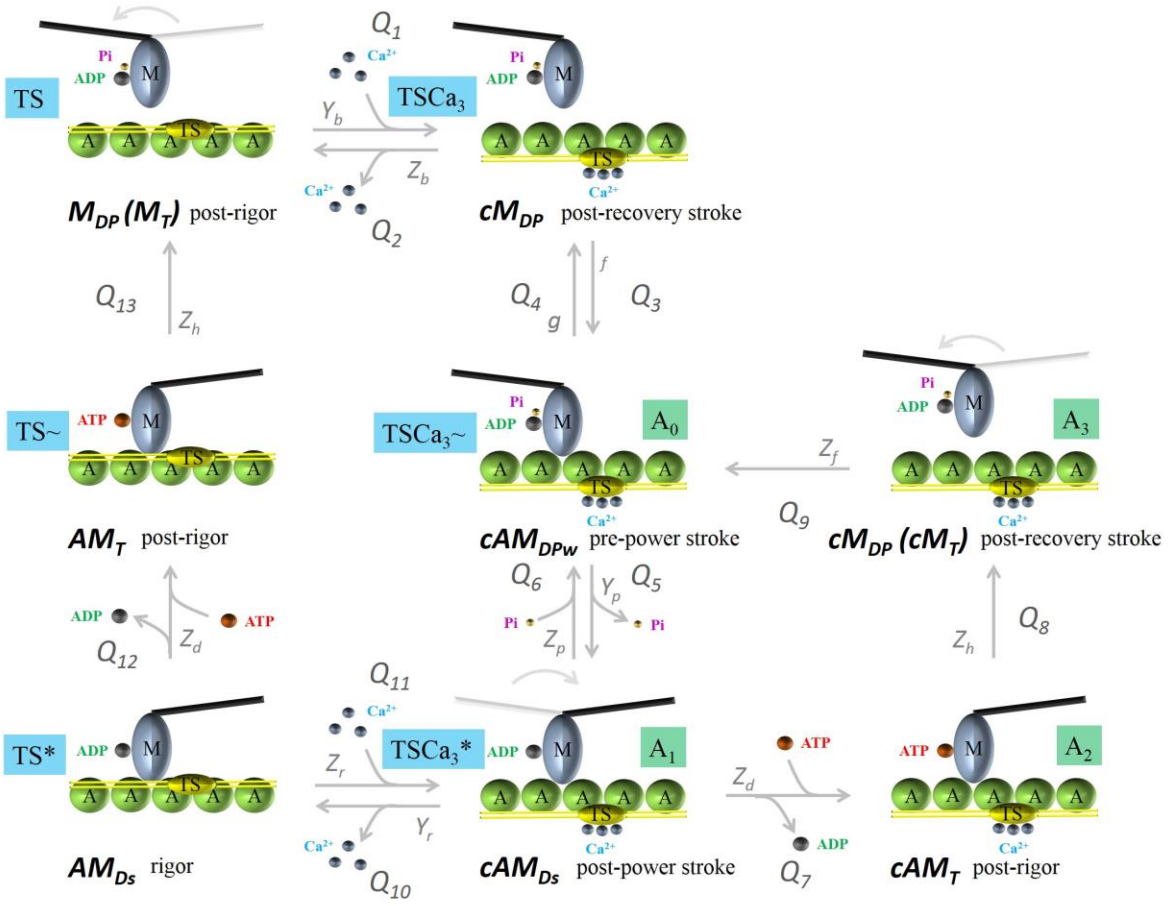

Figure 2-1 Eight-state transition model of new Hybrid model. Q_1 - Q_{13} define the flux of state transition. Rate *f* and *g* indicate attachment and detachment steps, respectively. Rate *Y* and *Z* indicate forward and reverse steps, respectively. The description of each state was described in Table 2-2. We noted that the 'Ca^{2+} tropomyosin gates' were located at Q_1-Q_2 and Q_{10}-Q_{11}.and the 'ATP gates' were locate at Q_7 and Q_{12}. The notation A_0 to A_3 indicates corresponding to lumped 4-state model (Månsson 2010, Månsson et al. 2015) illustrated in green square. The symbol of each state was located under each state.

[*A* = actin (green sphere), *M* = myosin (blue-gray ovoid), *c* = Ca^{2+} (blue-gray sphere), *T* = ATP (orange sphere), *D* = ADP (gray sphere), *P* = Pi (gold sphere), *w* = weak CB conformation, *s* = strong CB conformation].

The lumped 4-state biochemical model developed by Månsson (2010) well represents the four essential steps of the ATP-hydrolysis. These four states are represented by symbols of cAM_{DPw}, cAM_{Ds}, cAM_T, and cM_{DP} (cM_T), respectively, in the new state-transition scheme demonstrated in Figure 2-1, where letters *A, M, T, D, P, c* indicate actin, myosin, ATP, ADP, Pi and Ca^{2+}, respectively. Letters *w* and *s* indicate weakly- and strongly-bound conformations of CB, respectively. The correspondence of each state with the original A_0, A_1, A_2 and A_3 states defined in Månsson model is indicated in the green square at each state in the scheme.

More schematic composition of each state is indicated in the blue square with supplemental troponin system (TS) having a variable number of Ca^{2+}-binding sites (three sites in the NL model). Note that the Ca^{2+} binding sites are occupied in all of these four states in contrast to the three unoccupied states, AM_{Ds}, AM_T, M_{DP} (M_T) aligned on the left side relaxation pathway and connected with the same rate constants, Z_d, and Z_h, respectively, for simplicity. The angle of lever arm in connection to the S1 segment shows the conformation of myosin lever arm in the power stroke at cAM_{Ds} and the recovery stroke at cM_{DP} and M_{DP}. Thus, the Ca^{2+}-binding steps of Q_1-Q_2 and Q_{10}-Q_{11} as well as the CB attachment steps Q_3-Q_4 were adopted from the NL model, while the other steps of right part of the scheme (Figure 2-1) were all based on the Månsson model.

The new rate constants for these four Ca^{2+}-bound states of ATP hydrolysis were adjusted in this study to approximate overall rate of ATP hydrolysis in situ at the physiological temperature (Gibbs 1978, Suga 1990) referring to the theoretical ones determined as a function of ΔG of each conformation in the original Månsson model. The NL model is also well adapted to the kinetics in ventricular myocardium at 37°C. The time courses of the Ca^{2+} transient followed by the CB association and dissociation are quite similar to those observed in experimental finding (Lab et al. 1984). Under the systolic intracellular Ca^{2+} concentration ($[Ca^{2+}]_i$) of 0.5-1 μM at the physiological temperature, the rise of $[Ca^{2+}]_i$ and the Ca^{2+}-induced troponin-switch, corresponding step of M_{DP} to cM_{DP}, takes places within ~20 ms (Yue et al. 1986, Janssen et al. 2002).

The attachment (*f*) and detachment (*g*) rates of CB in the NL model are described by the following equations in the NL model (Huxley 1957, Negroni & Lascano 1996, 2008, Negroni et al. 2015) equations 1 and 2, respectively, as a function of the half sarcomere length (*halfSL*) or the eCB elongation at weak state (h_w) to reconstruct the transient kinetics evoked by applying rapid changes in length or external mechanical load.

$$f = Y_a \cdot e^{-Ra\cdot(halfSL-La)^2} \qquad \text{Eq. 1}$$

$$g = F_h \cdot Y_v \cdot \left(1 - e^{-\gamma\cdot(h_w - h_{wr})^2}\right) + Z_a \qquad \text{Eq. 2}$$

$$F_h = \begin{cases} 0.1 & ; h_w > h_{wr} \\ 1 & ; h_w \le h_{wr} \end{cases} \qquad \text{Eq. 3}$$

Rate *f* depends on *halfSL* where *La* refers to the optimal overlap length at maximum level of CB attachment and *Ra* establishes the kurtosis of the curve. Y_a is maximum of rate *f* when *halfSL* equals to *La*. The function of $(1-e^{-\gamma\cdot(h_w-h_{wr})^2})$ in equation 2 represents the symmetrical detachment, while F_h provides asymmetry in equation 3 postulated by Huxley (1957). Y_v amplifies the detachment effect. The γ defines the kurtosis of curve and Z_a is an involved parameter. The h_w and h_{wr} indicate mean and steady elongation of attached CBs in weak state, respectively.

In the original NL model (2008), the state transition from M_{DP} to cM_{DP} represents the lumped step of Ca^{2+} binding to troponin and the subsequent conformation change in the tropomyosin complex. Therefore, this step was conserved as in the original model to make the merit of the NL model. In the original model, virtually simultaneous binding of three Ca^{2+} to sequential Ca^{2+}-binding sites on actin filament (due to nearest neighbor influence) was assumed in accordance with the Hill criterion for cooperativity in the NL model, and a functional TS was assumed to consist of three sequential actin molecules. However, the resultant Hill coefficient was < 4 (close to 4) and still lower than the experimental value of 4-7 in the overall Ca^{2+}-F_b relationship in the experiments (Stehle & Iorga 2010). For those reasons, we newly readjusted the number of Ca^{2+} (*nCa*) bound to TS. We found that an assumption of simultaneous binding of five Ca^{2+} (*nCa* = 5) gave an overall Hill coefficient of 6-7 in the experimental Ca^{2+}-F_b relation (Chapter 2.2). Thus, the binding rate of Ca^{2+} to the TS is calculated as in equations 4 and 5.

$$Q_1 = Y_b \cdot [M_{DP}(M_T)] \cdot [Ca^{2+}]^{nCa} \quad \text{Eq. 4}$$

$$Q_{11} = Z_r \cdot [AM_{Ds}] \cdot [Ca^{2+}]^{nCa} \quad \text{Eq. 5}$$

A competitive interaction between ADP and ATP at the substrate binding site of myosin head is assumed with a limiting magnitude Z_d for both transition rates between Q_7 and between Q_{12} described in equation 6. The ATP consumption rate (v_{ATPase}) is calculated from two state transitions from cAM_{Ds} to cAM_T (Q_7) and from AM_{Ds} to AM_T (Q_{12}) (equations 7 to 9). All parameter rates are described in Table 2-3.

$$Z_d^* = \frac{Z_d}{\frac{K_{d,ATP}}{[ATP]} \cdot \left(1 + \frac{[ADP]}{K_{d,ADP}}\right) + 1} \quad \text{Eq. 6}$$

$$Q_7 = Z_d^* \cdot [cAM_{Ds}] \quad \text{Eq. 7}$$

$$Q_{12} = Z_d^* \cdot [AM_{Ds}] \quad \text{Eq. 8}$$

$$v_{ATPase} = nCa \cdot (Q_7 + Q_{12}) \quad \text{Eq. 9}$$

Table 2-3 Parameters for the CB state transitions in Hybrid model.

Parameter	Numerical value	Units
ADP	0.02	mM
ATP	6.67	mM
γ	28000	μm^{-2}
$K_{d,ADP}$	0.001	mM
$K_{d,ATP}$	0.001	mM
La	1.15	μm
[*mS1*]	120	μM
Ra	20	μm^{-2}
Y_a	0.00161	ms^{-1}
Y_b	0.07264	$\mu M^{-5}\ ms^{-1}$
Y_r	0.05588	ms^{-1}
Y_p	1.04775	ms^{-1}
Y_v	1.5	ms^{-1}
Z_a	0.00069	ms^{-1}
Z_b	0.07264	ms^{-1}
Z_d	0.36	ms^{-1}
Z_h	1.8	ms^{-1}
Z_f	0.9	ms^{-1}
Z_p	0.83800	ms^{-1}
Z_r	39.9443	$\mu M^{-5}\ ms^{-1}$

2.1.1 Magnitude of contraction and dynamics of equilibrium crossbridge elongation

In the NL model (2008), the converting factor (stiffness of elastic CB structure) of A_p and A_w were used to calculate the magnitude of developed tension for a unitary cross-section area of mm^2 of cardiac muscle for μM of the powered and weak CB concentrations, respectively. F_b is given by the pool of attach CB (the sum of weak CB force (F_{bw}) and powered CB force (F_{bp})) as the following equations with a dimension of mN/mm^2.

$$F_b = F_{bw} + F_{bp} \quad \text{Eq. 10}$$

$$F_{bw} = nCa \cdot A_w \cdot [cAM_{DPw}] \cdot h_w \quad \text{Eq. 11}$$

$$F_{bp} = nCa \cdot A_p \cdot ([cAM_{Ds}] + [AM_{Ds}]) \cdot h_p \quad \text{Eq. 12}$$

Here, the h_p and h_w represent the elongation of elastic component of strong-bound CB states (cAM_{Ds} and AM_{Ds}) and weak bound CB state (cAM_{DPw}), respectively. Note that the variable CB elongations within the whole population of CB within a cell are represented by a single eCB having an 'average' CB elongation, h_p and h_w for the powered and weak eCBs, respectively in the NL model. The rate of change in the eCB elongation, the amount of Ca^{2+} bound to the TS is calculated in the same way as in the original NL model. The force of the parallel elastic element (F_p) is given by equation 13.

$$F_p = K_e \cdot (halfSL - hSL_0)^5 + L_e \cdot (halfSL - hSL_0) \quad \text{Eq. 13}$$

K_e and L_e represent titin and cellular element elasticities for F_p normalized by cross-sectional area, respectively, and hSL_0 is slack length (*halfSL* when F_p equals to zero). The rate of change in the eCB elongation (h_w and h_p), the amount of Ca^{2+} bound to the TS is calculated with the correction factor *nCa*, essentially in the same way as in the original NL model.

halfSL is composed of two components; 1) a non-elastic component (*X*) and 2) an elastic component (*h*) which both compartments represent the weak (*w*) and the power (*p*) conformation. The sum of half sarcomere thick filament and the parts of the thin filament not overlapping either with thick filament indicated *halfSL* are given in equation 14 for power conformation and equation 15 for weak conformation that show the same *halfSL*.

$$X_p = halfSL - h_p \quad \text{Eq. 14}$$

$$X_w = halfSL - h_w \quad \text{Eq. 15}$$

The *X* length represents the movement of the eCB head along the actin filament. The rate of change in *X* (*dX/dt*) is given by equations 16 and 17 for power and weak conformations, respectively. The

B_w and B_p describe the equivalent CB kinetics in the weak and power states, respectively. The h_{pr} indicates steady elongation of attached CBs in the power work state. The parameter values are described in Table 2-4.

$$\frac{dX_p}{dt} = -B_p \cdot \left(h_p - h_{pr}\right) \quad \text{Eq. 16}$$

$$\frac{dX_w}{dt} = -B_w \cdot \left(h_w - h_{wr}\right) \quad \text{Eq. 17}$$

Table 2-4 Parameters for eCB.

Parameters	Numerical values	Units
A_p	2700	mN $mm^{-2}\mu m^{-1}\mu M^{-1}$
A_w	540	mN $mm^{-2}\mu m^{-1}\mu M^{-1}$
B_p	0.5	ms^{-1}
B_w	0.2[a]	ms^{-1}
h_{pr}	0.006	μm
h_{wr}	0.0001	μm
hSL_0	0.97	μm
K_e	105000	mN $mm^{-2}\mu m^{-5}$
L_e	10	mN $mm^{-2}\mu m^{-1}$

[a] B_w decreases 40% from original NL model

2.1.2 Concentration of myosin S1 segment and magnitude of contraction

The concentrations of all states in the scheme of state transition (Figure 2-1) are given in the terms of the TS. Thus, it is assumed that a single TS controls simultaneously a number *nCa* of CBs. The concentration of total myosin S1 segment ([*mS1*]) are given as,

$$[mS1] = [TS] \cdot nCa \quad \text{Eq. 18}$$

In the cell models so far published (Hunter et al. 1998, Jafri et al. 1998, Matsuoka et al. 2003, 2004, Coutu & Metzger 2005, Okada et al. 2005, Shim et al. 2007, 2008, Soltis & Saucerman 2010), variable troponin concentrations of ~70 μM were assumed. For the [*mS1*], a molar ratio of actin/troponin concentration of 7:1 (Potter 1974) and a ratio of myosin S1 segment/actin of 1:4.1 (Murakami & Uchida 1985) were reported in cardiac muscle. These findings give a ratio of myosin S1 segment/troponin of 1.71, or 119.7 μM [*mS1*] in the previous cell models. This value is well within the range of direct biochemical measurements of myosin head in ventricular tissue in various species, which are 200 (in pig, Kuhn et al.

1990), 157 (in guinea pig, Barsotti & Ferenczi 1988), and 144 μmole/kg wet weight (in rabbit, Hooijman et al. 2011). Here, we tentatively adopt the [*mS1*] = 120 μM.

2.1.3 Ca^{2+} transient for twitch contraction

The management of Ca^{2+} in mammalian cardiac cell is affected through the sarcoplasmic reticulum (Brutsaert et al. 1978) and the 7% of the sarcoplasmic reticulum is exchanged via Ca^{2+} channel (Sipido & Wier 1991). The idealized Ca^{2+} transient is produced by the release (Q_{rel}) of Ca^{2+} from the sarcoplasmic reticulum (SR) using the imposed time function and the uptake (Q_{pump}) of Ca^{2+} by the sarcoplasmic reticulum Ca^{2+}-v_{ATPase} on SR membrane (Carafoli 1985, Peterson et al. 1991, Sipido & Wier 1991, Negroni & Lascano 1996, 2008, Campbell et al. 2001, Rice et al. 2003). Both of release and uptake are functions of time (t). The equations are described as following equations.

$$Q_{rel} = Q_m \cdot \left(\frac{t}{\tau_r}\right)^4 \cdot \exp\left(4 \cdot \left(1 - \frac{t}{\tau_r}\right)\right) + \frac{K_p}{1 + \left(\frac{K_m}{Ca_{rest}}\right)^2} \qquad \text{Eq. 19}$$

$$Q_{pump} = \frac{K_p}{1 + \left(\frac{K_m}{[Ca^{2+}]}\right)^2} \qquad \text{Eq. 20}$$

The Q_m, τ_r, K_m, K_p, and Ca_{rest} are related parameter described in Table 2-5. The free Ca^{2+} concentration ($[Ca^{2+}]$) is calculated by equation 21, which includes Q_{rel} and Q_{pump}, and the binding and releasing by troponin (Q_1, Q_2, Q_{10}, Q_{11}).

$$\frac{d[Ca^{2+}]}{dt} = Q_{rel} - Q_{pump} + \left(0.3 \cdot nCa \cdot \left(Q_2 - Q_1 + Q_{10} - Q_{11}\right)\right) \qquad \text{Eq. 21}$$

Table 2-5 Parameters for Ca^{2+} dynamics.

Parameter	Numerical value	Units
Ca_{rest}	0.1	μM
K_m	0.2	μM
K_p	0.15	μM ms^{-1}
Q_m	3.2	μm
τ_r	8	ms

2.1.4 Implementation in the multi-scale of cardiovascular system

We implemented our Hybrid model with Laplace's left ventricular hemispherical model (Moriarty 1980) and a lumped blood circulation parameter model illustrated in the diagram (Figure 2-2). Mathematically, the cell tension or force generation (F_b; CB force, F_p; parallel force) from hybrid model is used for the calculation of the ventricular pressure using the simplified half-hemispheric ventricle based on Laplace's law. The Law describes the relation of left ventricular between pressure (p_{LV}), wall thickness (h_{LV}), wall tension (F_{ext}), and radius (r_{LV}) given by equations 22 and 23. The p_{LV} is given by the relationship of the left ventricular wall thickness at end systolic point (h_{LVES}) and at end diastolic point (h_{LVED}) and the tension in wall subsequently defined at end systolic (F_{bES}) and at end diastolic (F_{bED}) using the value of force from our hybrid model (equation 24). The change in left ventricular volume (v_{LV}) is calculated from the flow parameter of the lumped parameter model of cardiovascular hemodynamics (equations 25-28). The value of v_{LV} is used to calculate *halfSL* using the simplified ventricle model represented as the left ventricular radius (r_{LV}) (equations 29 and 30). The *halfSL* provided from ventricle model sends the new value back to Hybrid model, to generate force. All parameter values were modified to fit this new simple model of cardiovascular system (Table 2-6).

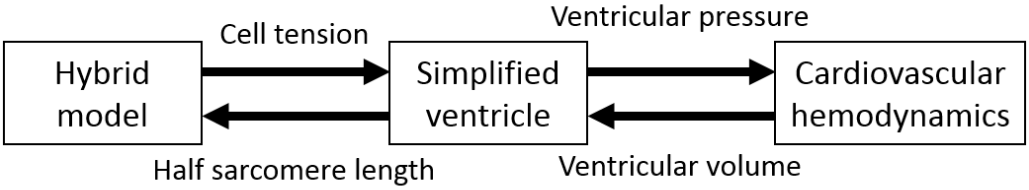

Figure 2-2 The integration of hybrid model with simple model of cardiovascular system.

$$\frac{p_{LV}}{h_{LV}} = \frac{2 \cdot F_{ext}}{r_{LV}} \qquad \text{Eq. 22}$$

$$F_{ext} = K_u \cdot (K_s \cdot F_b + F_p) \qquad \text{Eq. 23}$$

$$h_{LV} = \frac{F_b - F_{bED}}{F_{bES} - F_{bED}} \cdot (h_{LVES} - h_{LVED}) + h_{LVED} \qquad \text{Eq. 24}$$

$$q_0 = \begin{cases} \dfrac{P_{E1} - p_{LV}}{Rpv \cdot K_{rp}} & ; p_{LV} < P_{E1} \\ 0 & ; p_{LV} \geq P_{E1} \end{cases} \qquad \text{Eq. 25}$$

$$q_{in} = \begin{cases} \dfrac{p_{LV} - P_a}{Rlo} & ; p_{LV} > P_a \\ 0 & ; p_{LV} \le P_a \end{cases}$$ Eq. 26

$$\frac{dP_a}{dt} = \frac{q_{in} - \dfrac{P_a - P_{E2}}{R_{out}}}{Cds}$$ Eq. 27

$$\frac{dv_{LV}}{dt} = q_0 - q_{in}$$ Eq. 28

$$r_{LV} = \left(\frac{v_{LV} - V_\gamma}{K_\beta} \right)^{\frac{1}{K_\alpha}}$$ Eq. 29

$$halfSL = r_{LV} \cdot K_L + L_b$$ Eq. 30

Table 2-6 Parameters for simple model of cardiovascular system.

Parameter	Value	Description
Cds	1.5	Scale factor parameter
F_{bED}	0.05	Left ventricular wall tension (or F_b) at end diastolic point
F_{bES}	3.5	Left ventricular wall tension (or F_b) at end systolic point
h_{LVED}	10	Left ventricular wall thickness at end diastolic point
h_{LVES}	17	Left ventricular wall thickness at end systolic point
K_α	3.920469355	r_{LV}-v_{LV} relationship parameter
K_β	2.329855402	r_{LV}-v_{LV} relationship parameter
K_L	0.2173898347	Proportional constant of the relationship between *halfSL* & r_{LV}
K_R	0.012	Scale factor parameter
K_{rp}	1	Scale factor parameter
K_s	2.5	Ratio of cardiac cell to ventricular wall tension
K_u	7.50064	Scale factor parameter
K_V	1.478467483	Scale factor parameter
L_b	0.4927578979	*halfSL*-intercept of the relationship between *halfSL* and r_{LV}
P_{E1}	10	Left ventricular pressure parameter
P_{E2}	15	Left ventricular pressure parameter
Rlo	1	Scale factor parameter
R_{out}	1050	Scale factor parameter
Rpv	27	Scale factor parameter
V_γ	35	r_{LV}-v_{LV} relationship parameter

2.1.5 Time-integration of ordinary differential equations

The numerical integration was performed by Euler's method. The Ca^{2+} transient was generated by the empirical equations given in the NL model (Negroni & Lascano 2008). The model parameters and equations were described in Supplementary Materials. Following dimensions were applied; μM for concentrations, ms for time, mN/mm^2 for force of contraction, μm for length, mmHg for pressure, and ml for volume. All codes of the simulation program were prepared using Microsoft Visual Basic on Visual Studio Community 2013.

2.2 Characteristic of new Hybrid model

The cycle of actomyosin ATPase is maintained by Ca^{2+} and is relevance with F_b. The actomyosin (AM) ATPase is activated indirectly by Ca^{2+}, and repetitive cycles of hydrolysis are maintained in the presence of $[Ca^{2+}]$. The rate of ATP hydrolysis with accompanying developed tension F_b is examined by applying various $[Ca^{2+}]$ to the hybrid model. Since the magnitude of F_b is dependent on *halfSL*, the relationship between $[Ca^{2+}]$ and the rate of ATP-hydrolysis is examined at different *halfSL* (Figure 2-3; Panel A and C). It seems that these dose-response relationships well conform to a Hill's equation, although the underlying state transitions following the Ca^{2+} binding, including A_0-A_3 steps are quite complicated (Figure 2-1). To compare with the experimental $[Ca^{2+}]$-F_b relationship obtained by Kentish et al. (1986), and Gwathmey & Hajjar (1990), the Hill coefficient is measured by modifying the Hill equation in a linear form of relationship for F_b or ATPase activity (v_{ATPase}) with $V_{max,\,Fb}$ or $V_{max,\,ATPase}$, respectively (equations 31 and 32). The results of those relationships were described in Figure 2-3 and Table 2-7.

$$\ln\left(\frac{V_{\max,Fb}}{F_b}-1\right)=-n_H\cdot\ln\left(\frac{[Ca^{2+}]}{K_{0.5}}\right) \qquad \text{Eq. 31}$$

$$\ln\left(\frac{V_{\max,ATPase}}{v_{ATPase}}-1\right)=-n_H\cdot\ln\left(\frac{[Ca^{2+}]}{K_{0.5}}\right) \qquad \text{Eq. 32}$$

Table 2.7 The relationship of Ca^{2+} with F_b and v_{ATPase} in different *halfSL*.

	halfSL 0.8 μm	*halfSL* 0.9 μm	*halfSL* 1.0 μm	*halfSL* 1.1 μm
F_b at maximum (mN/mm^2)	229.57	436.33	554.69	598.31
v_{ATPase} at maximum (μM/ms)	5.07	9.63	12.24	13.20
$K_{0.5}$ (μM)	1.083	0.980	0.905	0.852
n_H	5.949	6.466	6.920	7.238

Figure 2-3 (Panel B & D) shows approximately linear relationships. The slope of those relationships is determined as a mean n_H over an interval of -0.3 to 0.3 on the abscissa (red dotted lines in Figure 2-3; Panel B & D). If the relative amplitudes are compared between these values, $V_{max,ATPase}$ is quite proportional to $V_{max,Fb}$. The slope of the relationship become slightly shallower with increasing [Ca^{2+}], mostly due to the limited number of TS. Note the cooperativity is assumed only for the Ca^{2+} binding to troponin. These results are all quite consistent with the experimental findings.

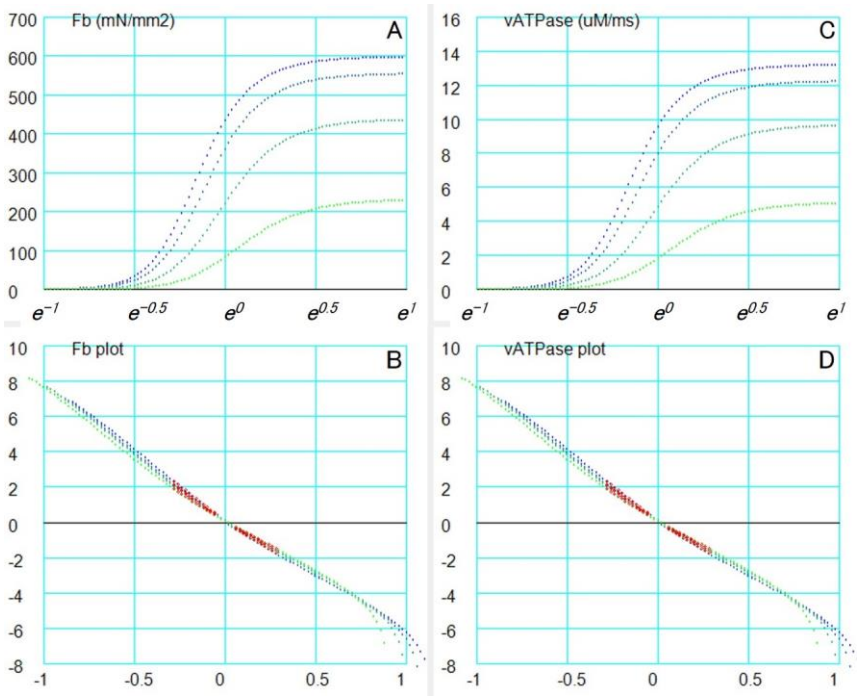

Figure 2-3 The linear relationship of Ca^{2+} with F_b and v_{ATPase} in different *halfSL*. The slope of the relationship in red dotted line (Panel B & D) indicates a mean n_H over an interval of -0.3 to 0.3. The x-axis of Panel A & C indicates Ca^{2+} concentration. The x-axis of Panel B & D indicates Ca^{2+} concentration from -1 to 1 of $ln([Ca^{2+}]/K_{0.5})$. The y-axis of Panel B & D indicates by $ln(V_{max,Fb}/F_b-1)$ and $ln(V_{max,ATPase}/v_{ATPase}-1)$, respectively. The gradient colors from green to blue dotted lines refer to *halfSL* 0.8, 0.9, 1.0, and 1.1, respectively.

Panel A; F_b-Ca^{2+} relationship, Panel B; non-linear relationship of F_b-Ca^{2+}, Panel C; v_{ATPase}-Ca^{2+} relationship, Panel D; non-linear relationship of v_{ATPase}-Ca^{2+}

2.2.1 The ATP hydrolysis activated by [Ca^{2+}] in the new Hybrid contraction model

The proportionality between F_b and v_{ATPase} in Figure 2-3 is expected in the present Hybrid model. Namely, both F_b and v_{ATPase} are largely determined by [cAM_{Ds}] and [AM_{Ds}] in both equations 12 and 33, respectively. The first term in equation 11, representing the contribution of weak bound CB, is a minor component of the total F_b during the steady presence of Ca^{2+} because the h_w quickly relaxes to a negligibly small h_{wr} (=0.0001 μm). It might be noticed that the denominator in equation 33 is constant since [ATP] and [ADP] are both given constant during the time course in the Figure 2-3. From equations 6 to 9, the v_{ATPase} can be rewritten as equation 33.

$$v_{ATPase} = nCa \cdot \frac{Z_d \cdot \left([cAM_{Ds}] + [AM_{Ds}]\right)}{\frac{K_{d,ATP}}{[ATP]} \cdot \left(1 + \frac{[ADP]}{K_{d,ADP}}\right) + 1} \qquad \text{Eq. 33}$$

The ATPase activity is examined during the usual developed tension evoked by the Ca^{2+} transient at a *halfSL* = 1.05 µm (Figure 2-4). The model is activated by the standard Ca^{2+} transient given by equations 19 and 20. The component of AM_T is not included in the calculation of F_b, since this state in the new hybrid model represents a sum of (AM_T + M_T) in Månsson A_2 and A_3 states. In Figure 2-4 (Panel D), the time course of v_{ATPase} is nearly similar to that of F_b in panel B (Figure 2-4). During a single stimulus interval of 800 ms, the amount of ATP used is 403 µM, which gives an average of ATPase turnover of 3.36 s^{-1} (=403 / 120). The peak turnover rate is 14.74 s^{-1}. The ATP consumption rate via transition step Q_{12} during the removal of Ca^{2+} is much smaller if it is compared with the step Q_7.

The turnover rate of the ATP hydrolysis was estimated by measuring the enthalpy output in rat trabeculae by Widén and Barclay (2006) using the myothermic technique (Woledge 1998). On the basis of one ATP molecule is hydrolyzed in each cycle of CB, they concluded a 0.5 turnover of the cycle during a single twitch contraction at 27ºC. If the temperature coefficient (Q_{10}) of 3.5 is assumed, a turnover of 1.75 / twitch is expected at 37 ºC. They suggested that this data might be determined by the magnitude of Ca^{2+} transient.

A clear dependency of turnover / twitch on the peak [Ca^{2+}] of the Ca^{2+} transient is observed by varying Q_m in equation 19 as indicated in the Table 2-5. The turnover rate (1.7449 / twitch), similar to the experimental 1.75 / twitch is obtained with a peak Ca^{2+} of 1.14 µM Ca^{2+}, which is quite agreeable with the usual size of the Ca^{2+} transient in cardiac myocytes. In Hybrid model, the changes in the peak of Ca^{2+} concentration using the adjusted values of Q_m have a great impact to ATP turnover / twitch (Table 2-8).

Table 2-8 The measurement of turnover / twitch from this hybrid model.

Q_m	peak Ca^{2+} (µM)	turnover / twitch (s^{-1})
1	1.3291	3.3636
0.9	1.2259	2.5482
0.8	1.1530	1.8660
0.7	1.0924	1.3092
0.6	1.0362	0.8688
0.5	0.9799	0.5347

2.2.2 Hydrolysis of ATP at isometric contraction modes

The result of isometric contraction with Ca^{2+} transient was illustrated in Figure 2-4. The maximum of F_b is 80.2 mN/mm^2 and the total of ATP consumption is 403.61 μM / cycle. The ATP turnover rate is 14.11 /s and 14.75 /s at 200-300 ms and at maximal value. Peak Ca^{2+} transient was 1.3291 μM.

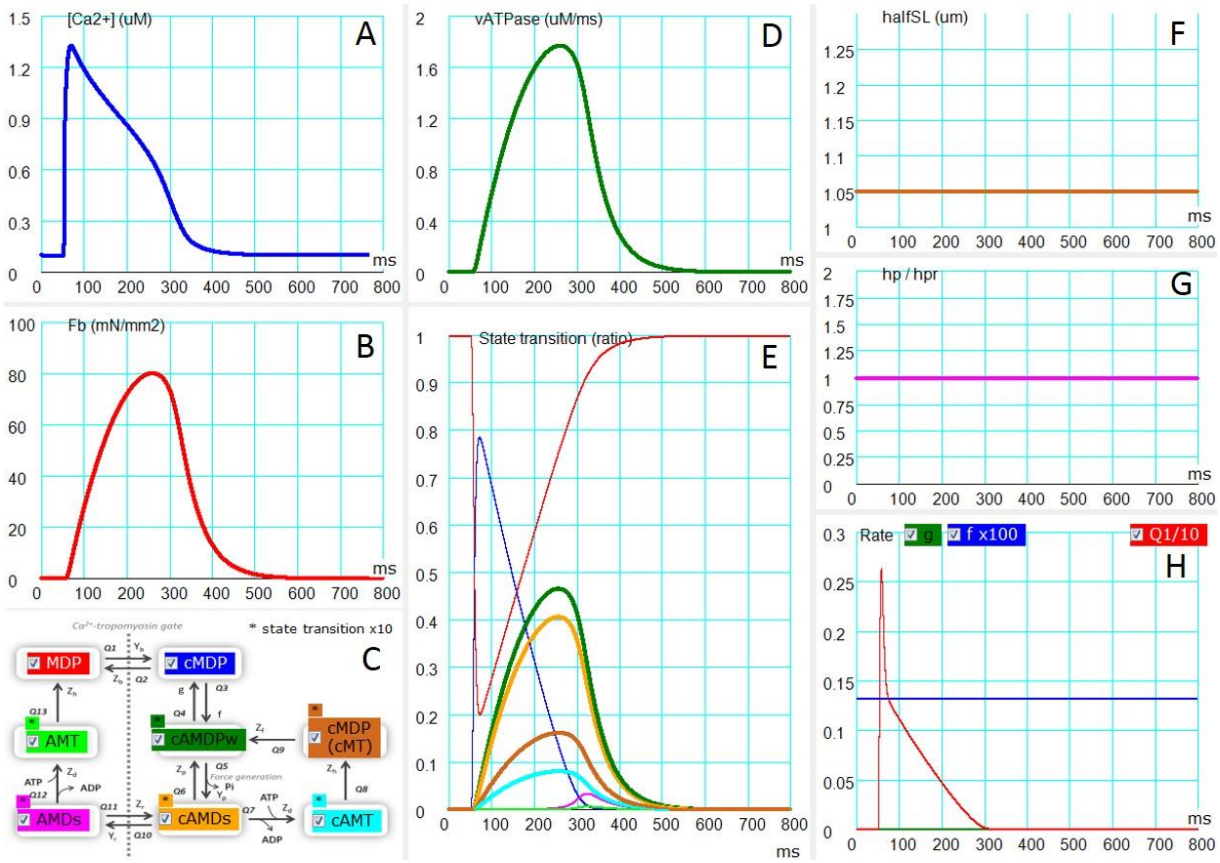

Figure 2-4 Hydrolysis of ATP during the isometric contraction evoked by the Ca^{2+} transient. The x-axis indicates the time course (ms).

Panel A; Ca^{2+} concentration (μM), Panel B; F_b (mN/mm^2), Panel C; eight-state transition scheme, Panel D; v_{ATPase} (μM), Panel E; the state transition (μM) from panel C, Panel F; *halfSL* (1.05 μm), Panel G; h_p / h_{pr}, Panel H; rate g (green) & f (blue; × 100) (ms^{-1}) and Q_1 (/ 10, μM)

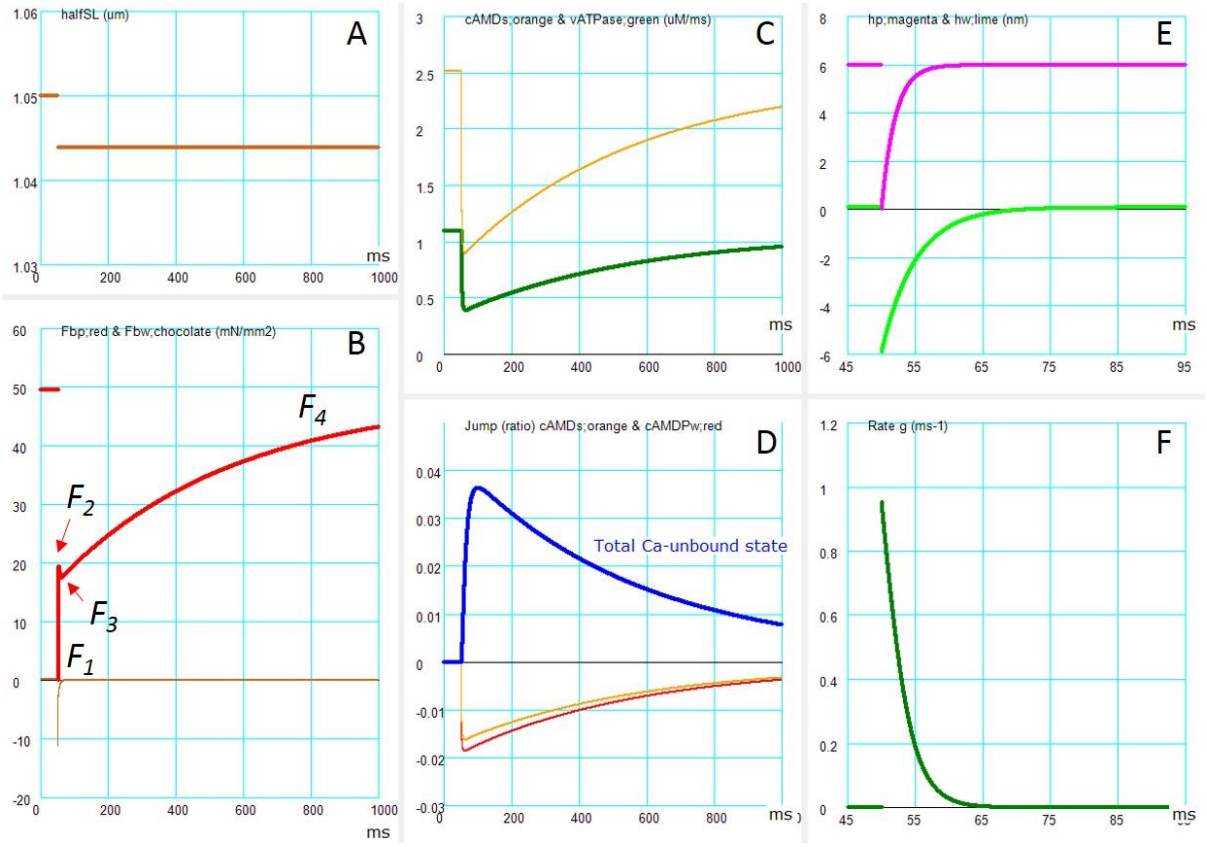

Figure 2-5 The ATP hydrolysis rate during the length step experiment under the isometric contraction mode. The notation of different phases of relaxation, F_1-F_4, is indicated in Panel B. The [Ca^{2+}] is 0.647 µM.

Panel A; *halfSL* (µm), Panel B; F_{bp} (red) & F_{bw} (chocolate) (mN/mm^2), Panel C; [cAM_{Ds}] (orange) & v_{ATPase} (green) (µM), Panel D; jump (ratio) of [cAM_{Ds}] (orange) & [cAM_{DPw}] (red) and total Ca^{2+}-unbound state (µM) (blue), Panel E; h_p (magenta) & h_w (lime) (nm), Panel F; rate g (ms^{-1})

The measurements of relaxation time course evoked by applying a step change in *halfSL* during *halfSL*-controlled conditions, provide essential parameters for the kinetics of the state transitions of the eCB conformations. Thus, we test our new model by reconstructing the length step experiment and examine the ATP-hydrolysis under this experimental condition. In the simulation in Figure 2-5, the simulation tests the application of 6 nm shortening of *halfSL* at a constant [Ca^{2+}] of 0.647 µM. At the onset of the length step of 6 nm, h_p and F_{bp} decrease to ~0. Thereafter, h_p largely recovers within the subsequent 5 ms because of the rapid intrinsic rate of dh_p/dt (from F_1 to F_2 level illustrated in Figure 2-5; Panel B). The simultaneous negative deflection of h_w causes a rapid detachment of the eCB by 65% according to equation 2 (Figure 2-5; Panel C) through the transient increase in g (Figure 2-5; Panel F). These rapid transient changes (F_2 and F_3 in Figure 2-5; Panel B) last within ~10 ms. The F_4 phase of the F_b recovery lasts ~600 ms due to the re-equilibration of state transitions as in the original NL model. The time course of v_{ATPase} change is largely parallel to the time course of [cAM_{Ds}] as shown in green and orange lines, respectively (Figure 2-5; Panel C). This finding indicates that the ATP consumption should be transiently

decreased at the onset of the shortening length pulses are applied. Thereafter, the ATPase activity will largely recover during the F_4 phase.

2.2.3 Hydrolysis of ATP at isotonic contraction modes

The result of isometric contraction with Ca^{2+} transient was illustrated in Figure 2-6. The maximum of F_b is 56 mN/mm^2 and the total of ATP consumption is 289.14 μM / cycle. The ATP turnover rate is 9.91 /s and 10.39 /s at 200-300 ms and at maximal value. Peak Ca^{2+} transient is 1.3291 μM. The isotonic contraction is characterized by the delayed peak in the developed tension F_b and the ATP flux if it is compared with the isometric contraction. This delayed peak is caused by the shortening of h_p and thereby *halfSL* (Figure 2-6) in contrast to the isometric contraction. This decrease in h_p largely inverted h_w at the onset of contraction followed by gradual relaxation toward the stable length of h_w (0.0001 μm) during contraction. Thus, the CB detachment rate g, given as a function of h_w deviation from h_{wr} (Equation 2), is largely increased (Figure 2-6; Panel H). On the other hand, the attachment rate f is nearly constant, though increased only slightly. Through these changes in the CB kinetics, the development of cAM_{Ds} is largely delayed and its magnitude is smaller, if it is compared with the isometric contraction. Thereby, the peak tension and the peak of v_{ATPase} are delayed according to the time course of the cAM_{Ds} state. Note the AM_{Ds} becomes a significant component only during the late relaxation phase (Figure 2-6).

The [cAM_{Ds}] is increased according to equation 5. Thereby, the peak tension and the peak of v_{ATPase} are delayed according to the time course of the state cAM_{Ds}. Comparison of the falling phase of v_{ATPase} with that of F_b shows clearly earlier peak of the v_{ATPase} than F_b and v_{ATPase} relaxes earlier than that of F_b. This difference is explained by the larger weight (Z_d = 0.36) of cAM_{Ds} than that of AM_{Ds} (Y_q = 0. 04656) in equation 12. The time course of F_b is quite similar to those in the original NL model (Negroni & Lascano 2008). Thus, it is evident that the addition of the ATP hydrolysis cycle to the NL model does not affect the general time course of contraction obtained in the new Hybrid model.

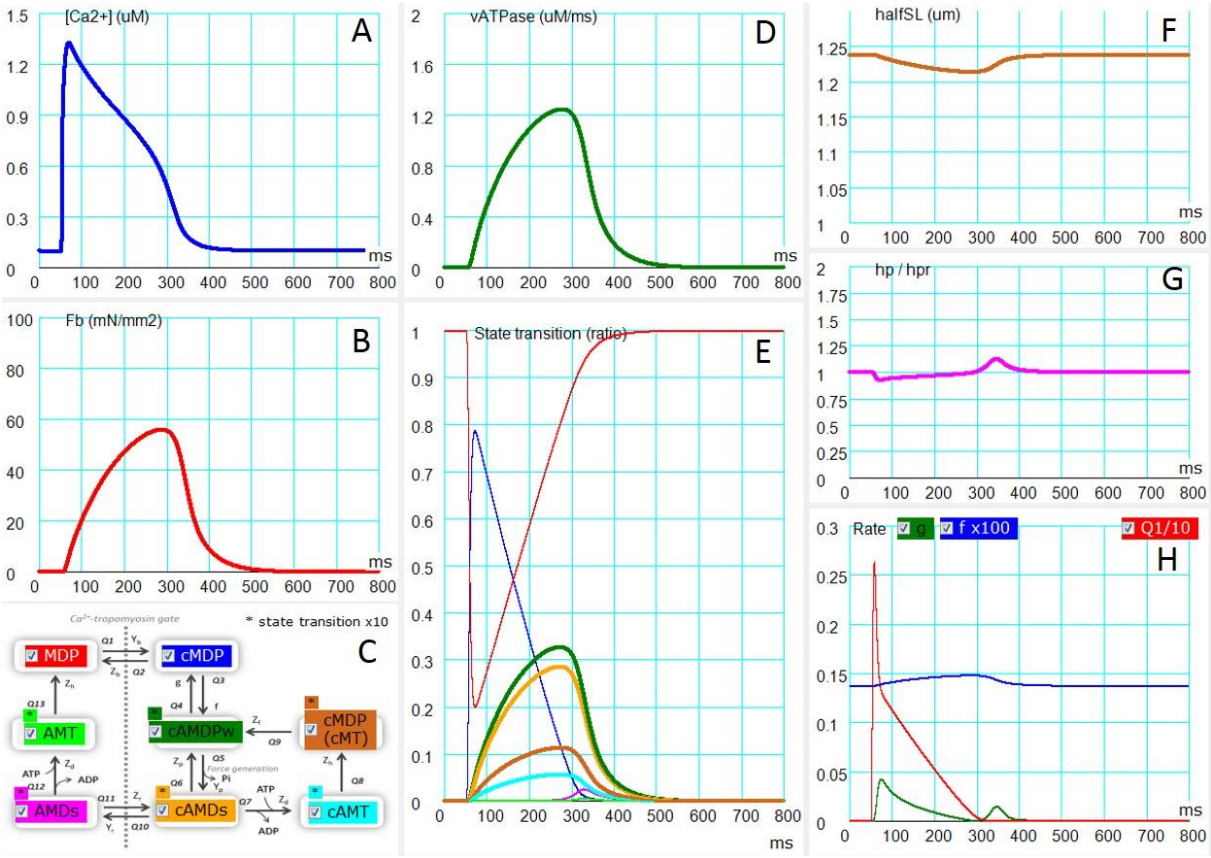

Figure 2-6 Hydrolysis of ATP during the isotonic contraction evoked by the Ca^{2+} transient. External force is 150 mN/mm^2.

Panel A; Ca^{2+} concentration (µM), Panel B; F_b (mN/mm^2), Panel C; eight-state transition scheme, Panel D; v_{ATPase} (µM), Panel E; the state transition (µM) from panel C, Panel F; *halfSL* (µm), Panel G; h_p / h_{pr}, Panel H; rate g (green) & f (blue; × 100) (ms^{-1}) and Q_1 (/ 10, µM)

The rapid release experiment reveals the four phases in the time course of *halfSL* shortening, characterized by the initial jump (phase 1), the rapid hyperbolic shortening (phase 2) within the initial 50 ms, the subsequent slow almost linear shortening (phase 3), and steady decline (phase 4) as observed, typically in the skeletal muscle (Figure 2-7; Panel B). This simulation results are quite comparable to the relaxation time course to the original one in NL model (Negroni & Lascano 1996, 2008). Similar time courses were typically observed in experiments in cardiac muscles, but obviously, at low time resolution because of the intrinsic complexity of the trabeculae in the cardiac tissue (de Tombe & ter Keurs 1991).

The force clamp experiment is quite straightforward, namely the product of h_p multiplied by the number of eCB is proportional to the applied load (F_{ext}). The quick release instantaneously decreases h_p (upper line, Figure 2-7; Panel D) or negative deflection of h_w (lower line, Figure 2-7; Panel D). The deviation in h_w from h_{wr} decreases the number of attached eCB by accelerating the rate of detachment (g) of eCB represented by equation 2 like in the length pump simulation. This decrease in the number of eCB increases h_p to balance the applied F_{ext}. Through these two opposite influences of decreasing and increasing h_p, the magnitude of h_p relaxes approximately to a new steady level during the phases 1-2. The fraction of cAM_{Ds} reaches a new equilibrium level through almost simple sigmoidal time course. Therefore, the rate of ATP-hydrolysis is almost linearly related to the level of test external load during the phase 3, as shown in Panel F (Figure 2-7), differently from the length clamp experiment.

It should be noted that the magnitude of h_p remains nearly equal to 6 nm during the phase 4 shortening. This means that the shortening of *halfSL* is attributable exclusively to the movement of eCB attachment point along the actin fiber. The rate of shortening in phase 4 is nearly an exponential function of the mechanical load in Panel E (Figure 2-7) in rough agreement with experimental findings.

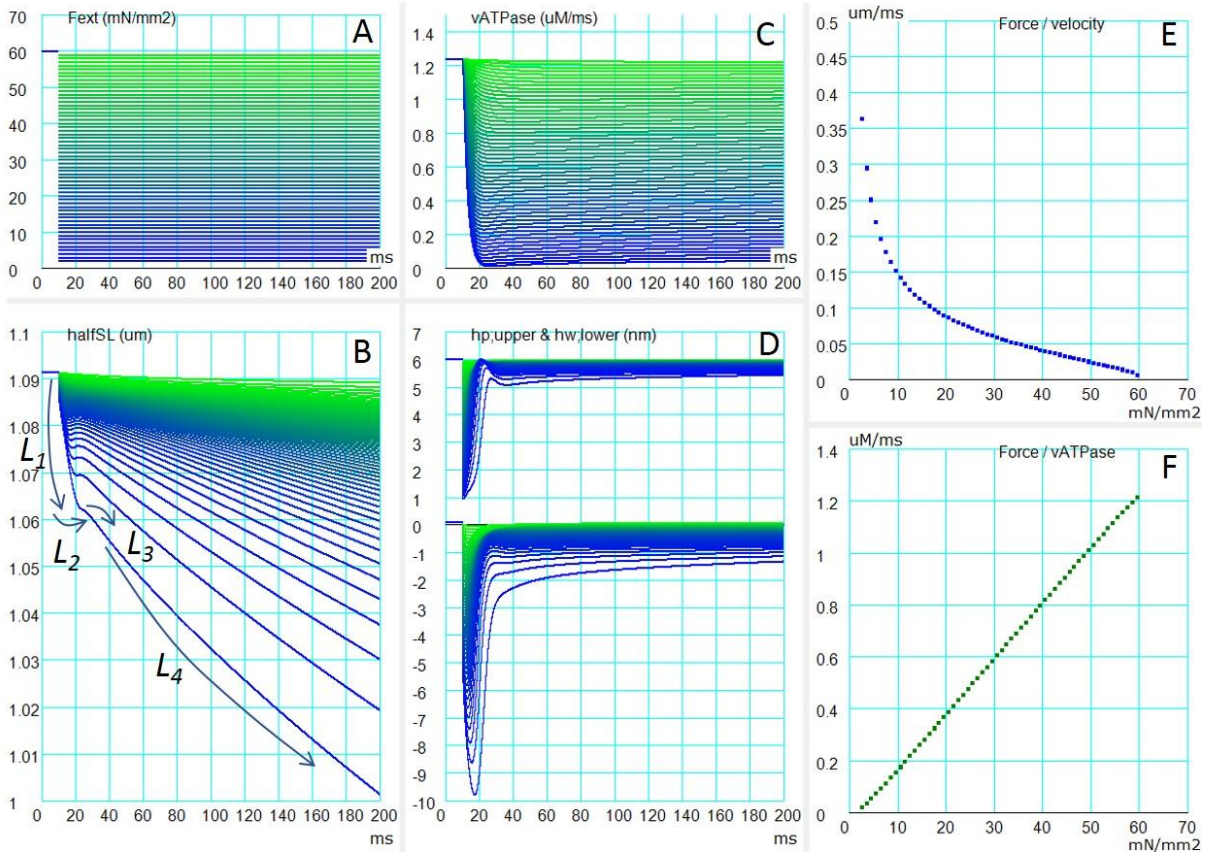

Figure 2-7 The ATP hydrolysis rate during the step experiment under the isotonic contraction mode. Panels A-D, the gradient color lines from green to blue are used, referring to the step size of F_{ext}, as obvious in Panel A, during the test pulse. The rates in Panels E and F are measured between 79-80 ms. The notation of different phases of relaxation, L_1-L_4, are indicated in Panel B (F_{ext} from 60 → 2 mN/mm^2). The [Ca^{2+}] is 0.647 µM.

Panel A; F_{ext} (mN/mm^2), Panel B; *halfSL* (µm), Panel C; v_{ATPase} (µM), Panel D; h_p (upper line) & h_w (lower line) (nm), Panel E; F_{ext} / velocity (dh_p/dt) relationship, Panel F; Load (F_{ext}) / v_{ATPase} relationship

2.2.4 Integration of present Hybrid model in the simple blood circulation model

The NL model have been used to examine the hemodynamics in the multi-scale model of cardiovascular system using 'Laplace's left ventricular hemispherical model (Moriarty 1980, Okada et al. 2005, Utaki et al. 2016). We replace the presented hybrid model for the original NL model in the hemodynamic model of Utaki et al (2016) (Figure 2-8).

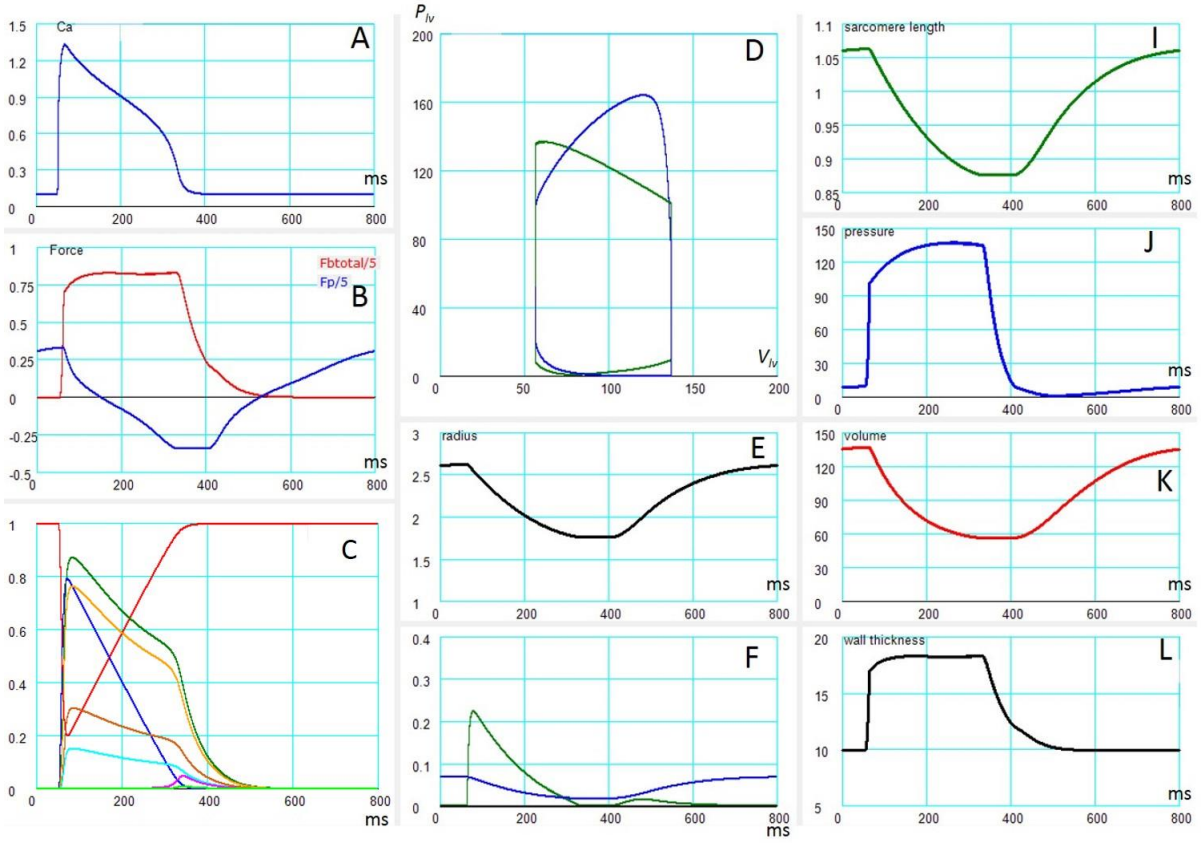

Figure 2-8 Multi-scale model of cardiovascular system.

Panel A; Ca^{2+} concentration (μM), Panel B; F_b (red) & F_p (blue) (mN/mm^2), Panel C; the state transition (μM) including [M_{DP} (M_T)] (red), [cM_{DP}] (blue), [cAM_{DPw}] (green), [cAM_{Ds}] (orange), [cAM_T] (cyan), [cM_{DP} (cM_T)] (chocolate), [AM_{Ds}] (magenta), and [AM_T] (lime), Panel D; p_{LV}-v_{LV} (green) and v_{ATPase}-v_{LV} (blue) relationship, Panel E; r_{LV} (mm), Panel F; rate g (green) & f (blue; × 50) (ms^{-1}), Panel I; *halfSL* (μm), Panel J; p_{LV} (mmHg), Panel K; v_{LV} (ml), Panel L; h_{LV} (mm)

We estimate the ATP consumption during the pressure-volume trajectory. As expected from the faithful reproduction of the developed tension described above (Figures 2-3 and 2-4), the pressure-volume trajectory obtained by the new system model seems to be quite consistent with the previous studies (Figure 2-9). The *PVA* of the left ventricle, which well correlates with the myocardial oxygen consumption per beat (Suga 1980), is varied (enlarged) by increasing the preload scale, standard K_{rp} ×0.6, ×0.8, ×1.0, ×1.2, and ×1.4 in Figure 2-9.

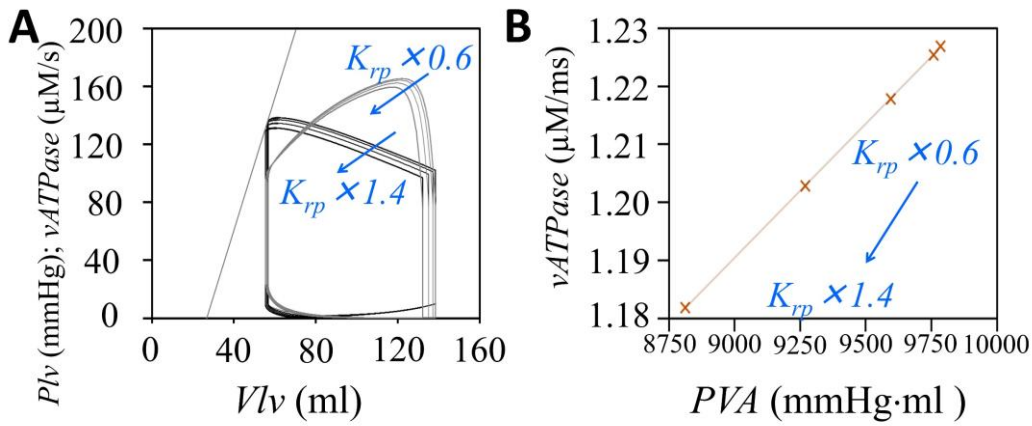

Figure 2-9 The ATP consumption of the Hybrid contract ion model during the pressure-volume relation of the hemisphere Laplace heart model. The preload scale factor K_{rp} is increased indicated by the arrow.
Panel A; The pressure-volume relationship (black line) and v_{ATPase}-volume (gray line) at different preload scale factors, Panel B; the linear relationship between *PVA* and the amount of v_{ATPase} per beat (orange cross marks)

The ATP usage of the hybrid contraction model is simultaneously plotted in the same figure, but at different scale (Figure 2-9; Panel A, depicted in gray). During the ejection period, the ATP hydrolysis rate decreases because of the decrease in the number of powered CB. This is different more than the gradual increase in the ventricular pressure, due to the decrease in the radius of the hemisphere Laplace heart. The relationship between *PVA* (mmHg × ml) and the corresponding integration of ATP usage (μM/ms) is examined in Panel B (Figure 2-9). The linear relationship between *PVA* and v_{ATPase} indicates the relevance of using the hybrid model in calculating the ATP consumption.

2.3 The summary of the present Hybrid contraction model

A new Hybrid contraction model is developed by combining the biochemical model elaborated by Månsson (2010) with the biophysical NL model (Negroni & Lascano 2008). The former is in succession to the foregoing dynamic CB models developed by Lombardi & Piazzesi (1990), Piazzesi et al. (1992), Edman et al. (1997) based on the tetanus contraction in skeletal muscle. On the other hand, the latter model of the TS reconstructs F_b in the cardiac myocytes over a wide variety of physiological experimental findings. In the new hybrid model, the scheme of the state transition among the A_0-A_3 states in the Månsson model is used as it is, but the rate constants for individual state transitions are simplified. In the original model, the rate was calculated by assuming a Gibbs free energy profile as a function of the distance (x) between the CB head and the nearest binding site on actin fiber. In the hybrid model, a constant rate is used for individual state transitions of eCB by referring to the rate change based on the Gibbs free energy profile. The new model well inherits the major characteristics of either type of the two models, such as the concentration-response relation of $[Ca^{2+}]$-F_b or $[Ca^{2+}]$-v_{ATPase} (Figure 2-3), the time course of the developed tension activated by the intracellular Ca^{2+} transient (Figures 2-4 & 2-6), the turnover rate of the AM ATPase, the F_b responses to jumps in the *halfSL* (Figure 2-5) and F_{ext} (Figure 2-7) under the isometric and isotonic contraction modes, respectively, and the load-velocity relation (Figure 2-7). When the new model is implemented in the hemodynamic blood circulation model, the ATP consumption is proportional to the *PVA* of the hemisphere Laplace heart (Figure 2-9).

2.3.1 Simultaneous reconstruction of the ATP consumption as well as the developed tension

As a minimum requirement, mathematical models of cardiac contracting fibers should capture following four essential steps of the CB cycle tightly coupled with the accompanying ATP-hydrolysis.

Step 1; The binding of ATP in place of ADP to the catalytic domain of the S1 segment rapidly detaches myosin head from actin binding site to relax the rigor state (Siemankowski & White 1984, Rayment et al. 1993, Spudich 1994, Yount et al. 1995).

Step 2; ATP is hydrolyzed associated with a structural change of a swing of the myosin lever arm (a recovery stroke), leaving products of ATP-hydrolysis, ADP and Pi bound to the active site of myosin head (Lymn & Taylor 1971, Rayment et al. 1993, Sugi et al. 2008).

Step 3; The Ca^{2+} binding to troponin dislocates tropomyosin complex during the Ca^{2+} transient within the cell (Ford 1991) and thereby allows the myosin head (carrying ADP and Pi) to bind with actin filament, forming a weakly bound state of CB (Shimizu et al. 1992, Spudich 1994).

Step 4; The attachment of the myosin head to the actin binding site causes ~100-fold increase of the rate of P_i release (Månsson et al. 2015). Dissociation of P_i from the S1 segment is tightly coupled with the power stroke of the CB, resulting in the sliding motion between the thin and thick filaments to stretch the elastic elements in the CB (Trentham et al. 1976, Geeves et al. 1984, Goldman 1987), which is responsible for the developed tension F_b.

The steps 1, 2 and 4 were precisely described in the biochemical models (Månsson model), while the NL model well simulated the step 3 based on biophysical experimental findings, such as the time

course of F_b evoked by the Ca^{2+} transient, the response of the shortening of the *halfSL* evoked by the rapid release protocol in the isotonic contraction, and the time course of F_b recovery evoked by the step shortening of the *halfSL* in the isometric contraction mode. The hyperbolic increase of shortening velocity with decreasing external load is reconstructed based on the time course of *halfSL* shortening reconstructed by the numerical integration in the model by applying the quick release protocol according to the experimental findings. In the Månsson model, this relationship was theoretically predicted indirectly from the state transitions.

The new hybrid model successfully calculates the rate of ATP hydrolysis simultaneously with the accompanying development of F_b. Thus, the presented hybrid model largely facilitates development of new whole cell models for analyzing the cardiac energetics, development of the force of contraction as well as the ATP dependency of the muscle contraction. The merit of using the NL model might be largely due to the introduction of the eCB, which represents the average behavior of the whole population of CBs within a cell. This kind of spatial average model of whole population of CBs has been used in variety of simplified models. In the NL model, the behavior of the eCB was thoroughly fitted to the classical experimental findings (Huxley & Simmons 1971, Huxley 1974, Ford et al. 1977, models; Izakov et al. 1991, Peterson et al. 1991, Landesberg & Sideman 1994). The time-dependent change of eCB elongation, h_p or h_w, is continuous as described in equations 16 or 17, and the rate g of detachment of CB is given as a function of h_w (Negroni & Lascano 2008, NL model) or h_p (Negroni & Lascano 1996, NL model). This g provides the basis of explaining the *halfSL*-dependence of the $[Ca^{2+}]$-F_b relationship (Kentish et al. 1986) (Figure 2-3). The relationship between the F_{ext} and dh_p/dt is also explained by the eCB kinetics, and the rate of quick recovery of F_b at the onset of the *halfSL* jump, and the time course of the shortening of *halfSL* evoked by the release of F_{ext}.

In the original model of Lombardi & Piazzesi (1990), fractions of CBs in A_1, A_2, and A_3 states were calculated by applying the numerical integration method with a discrete interval of (Δx) less than 0.5 nm at every x-points. It was also assumed that the elongation of CB was increased by an interval of the neighboring actin binding sites for each state transition of A_1-A_2, and A_2-A_3. When calculating the force–velocity relationship, the smooth continuous change in the velocity as well as force of CB were obtained theoretically by averaging for whole population of CB states without reconstructing the experimental response to quick release. Using a linear stiffness of the CB elongation, the force of contraction (for example with a unit of mN/mm^2) were calculated from the sum of A_2 (weak bound) + A_3 (strong bound) over the range of x.

Negroni & Lascano elegantly simplified the calculation of developed tension and the CB kinetics by assuming the eCB, which might be roughly represent the average CB elongation h_p or h_w, so the unitary developed tension (f_i) is calculated with a stiffness (a) of the elastic structure ($f_i = a \times h$), and the movement rate of the CB head along the actin fiber is calculated as dh/dt. The dh/dt is defined for both h_p and h_w as,

$$\frac{dh}{dt} = -B \cdot (h - h_r) \qquad \text{Eq. 34}$$

Note, equation 34 is equivalent with equation 16 provided that *halfSL* is constant during a time interval concerned, like in the phase L_4 in the isotonic contraction (Figure 2-7). Thus, dh_P/dt is used to calculate the movement of the CB head when attached. In the detached CB head, h relaxes quickly to the resting elongation (h_r). Note, the x_0 giving the energy minima in the detached A_3 state of the Månsson (2010) is about 7-8 nm apart from the corresponding position of energy minima in A_1 and A_2 state, which is close to h_r (= 6 nm) in the NL model, though Piazzesi et al. (1992) and Edman et al. (1997) assumed slightly different x_0 of energy minima. The binding rate was described as a function of the velocity of the CB head movement along the actin fiber in the Månsson model (2010). This assumption may correspond to the h-dependent detaching rate of g in the NL model.

The sequential steps of Q_7 - Q_9 and Q_{12} - Q_{13} are adopted from Månsson model, in which the weakly bound CB is separated from the powered CB according to experimental findings (Brenner et al. 1982, Geeves & Holmes 1999, Baumann et al. 2004, Ferenczi et al. 2005, Wu et al. 2010, Smith et al. 2008) and are combined with Q_1 - Q_4 and Q_{10} - Q_{11} steps of the 2008 version of the NL model. This modification does not largely modify the time course of developed tension if it is compared to NL model, because the newly implemented cycle of ATP-hydrolysis is much faster than in the entire state transition cycle in the original NL model. In the new hybrid model, the ATP-binding to the catalytic domain is also assumed in the Ca^{2+}-unbound state, AM_{Ds}, which appears during the relaxing phase shown in Figure 2-1. This assumption is justified by the recent finding that ATP-hydrolysis occurrs in the reconstructed myosin fiber in the absence of both Ca^{2+} and actin (Sugi et al. 2008). In our simulation (Figure 2-4), the contribution of AM_{Ds}, however, is only 3.5% of the total ATP consumption.

The ATP turnover rate of the new contraction model is 14.75 s^{-1} at the peak tension in Figure 2-4. This rate at the peak tension are roughly in the range of experimental measurements. Namely, quite consistent rates of 2.7-3.3 s^{-1} (Kentish & Stienen 1994, Ebus et al. 1994, Ebus & Stienen 1996) were reported in rat chemically skinned trabeculae in the presence of saturating concentration of Ca^{2+} at the room temperature (20-21ºC). If these rates are corrected for the physiological temperature using Q_{10} of ~3.5 obtained by de Tombe & Stienen (2007), an experimental turnover rate of 20-24 s^{-1} is expected, which is slightly larger than the simulation results. In the simulation shown in Figure 2-4, however, the development of the ATP flux is obviously interrupted by the decrease in $[Ca^{2+}]$, which is ~0.4 µM near the peak of ATP flux (300 ms). Thus, it may be concluded that the turnover rate of 20-24 s^{-1} obtained in the present human ventricular cell model is roughly in good agreement with the experimental values. It should be noted that the measurements of the turnover rate as well as Q_{10} showed variations. A much larger ATP turnover rate (~10 s^{-1} per myosin head at 24°C) was reported in skinned rat trabeculae (Wannenburg et al. 1997). On the other hand, a lower value was described in pig cardiac preparation, ~0.5 s^{-1} at 24°C (Kuhn et al. 1990) or in rat ~3 s^{-1} at 20°C using different experimental protocol (Ebus et al. 1994, Kentish & Stienen 1994, de Tombe & Stienen 1995, Ebus & Stienen 1996). Also, the temperature coefficient Q_{10} of ATP-hydrolysis were variable (Siemankowski et al. 1985, Q_{10} = ~5; Burchfield & Rall 1986, Q_{10} = ~4; de Tombe & Stienen 2007, Q_{10} = ~3.5). Species-specific differences in the ATP-hydrolysis rate might be attributed to differences in composition of isoforms of S1-myosin isoform (Stienen et al. 1996). While, the

original NL model has been proved that its kinetics are well adapted to the physiological temperature when incorporated in the whole cell models of guinea pig or human ventricular myocytes (Asakura et al. 2014, Himeno et al. 2015, Negroni et al. 2015).

2.3.2 Integration of the present Hybrid contraction model in ventricular cell model

We developed a human ventricular cell model that includes the detailed Ca^{2+}-induced Ca^{2+} release model and the contraction model in addition to the membrane excitation supported by the regulation of the intracellular ion concentration (Asakura et al. 2014, Himeno et al. 2015). However, the model which provides the measurement of ATP consumption during the muscle electrical excitation and contraction is not available.

When integrating the new hybrid model of contraction to analyze the energetics, the macroscopic measurements of ATP consumption might be referred because of its consistency. Usually it is estimated that the AM ATPase uses ~60% and other components including sarcoplasmic reticulum Ca^{2+}-ATPase (SERCA) and Na/K-ATPase use ~40% of the total ATP consumption under the physiological condition (Gibbs 1978, Suga 1990). Schramm et al. (1994) attributed 76% to actomyosin-ATPase and 15, and 9% to the SERCA and Na/K-ATPase, respectively. Note, the estimation of the ATP consumption from the ionic pump activities in the whole cell cardiac cell models is now well established by the refined magnitude of ionic fluxes underlying the membrane excitation (Grandi et al. 2010, O′Hara et al. 2011) as well as the Ca^{2+} fluxes underlying the cytosolic Ca^{2+} dynamics regulated by the sarcoplasmic reticulum (Hinch 2004, Asakura et al. 2014, Himeno et al. 2015). Thus, the magnitude of the ATP consumption by the AM ATPase might be safely adjusted in the whole cell model by referring to the fractional ATP consumptions. Theoretically, Han et al. (2012) compared the myocardial energetics proposed by Gibbs formalism (1978) based on heat (or enthalpy) measurement and Suga formalism (1980) based on the pressure-volume relationship. They assumed that the fundamental difference between Suga's phenological isoefficiency and Gibbs' load-dependent efficiency cannot be reconciled.

2.3.3 Limitation of the new Hybrid model

Taken together, the simulation results of the presented hybrid model are in good accordance to the experimental data so far published. However, the limitation of this new contraction mode is obvious, since the ability to generate realistic response does not prove that the underlying biophysical mechanisms are correctly represented.

2.4 References

Asakura K, Cha CY, Yamaoka H, Horikawa Y, Memida H, Powell T, Amano A, Noma A (2014) EAD and DAD mechanisms analyzed by developing a new human ventricular cell model. Prog Biophys Mol Biol 116:11-24

Barsotti RJ, Ferenczi MA (1988) Kinetics of ATP hydrolysis and tension production in skinned cardiac muscle of the guinea pig. J Biol Chem 263:16750-16756

Baumann BA, Liang H, Sale K, Hambly BD, Fajer PG (2004) Myosin regulatory domain orientation in skeletal muscle fibers: application of novel electron paramagnetic resonance spectral decomposition and molecular modeling methods. Biophys J 86:3030-3041

Brenner B, Schoenberg M, Chalovich JM, Greene LE, Eisenberg E (1982) Evidence for cross-bridge attachment in relaxed muscle at low ionic strength. Proc Natl Acad Sci USA 79:7288-7291

Brutsaert DL, de Clerck NM, Goethals MA, Housmans PR (1978) Relaxation of ventricular cardiac muscle. J Physiol 283:469-480

Burchfield DM, Rall JA (1986) Temperature dependence of the crossbridge cycle during unloaded shortening and maximum isometric tetanus in frog skeletal muscle. J Muscle Res Cell Motil 7:320-326

Campbell KB, Razumova MV, Kirkpatrick RD, Slinker BK (2001) Nonlinear myofilament regulatory processes affect frequency-dependent muscle fiber stiffness. Biophys J 81:2278-2296

Carafoli E (1985) The homeostasis of calcium in heart cells. J Mol Cell Cardiol 17:203-212

Cenci I, Morotti S, Negroni J, Rodriguez B, Severi S (2010) Mechano-electric feedback effects in a ventricular myocyte model subjected to dynamic changes in mechanical load. IEEE Comput Cardiol 37:193-196

Coutu P, Metzger JM (2005) Genetic manipulation of calcium-handling proteins in cardiac myocytes. II. Mathematical modeling studies. Am J Physiol Heart Circ Physiol 288:H613-H631

de Tombe PP, Stienen GJM (1995) Protein kinase A does not alter economy of force maintenance in skinned rat cardiac trabeculae. Circ Res 76:734-741

de Tombe PP, Stienen GJM (2007) Impact of temperature on cross-bridge cycling kinetics in rat myocardium. J Physiol 584:591-600

de Tombe PP, ter Keurs HE (1991) Sarcomere dynamics in cat cardiac trabeculae. Circ Res 68:588-596

Ebus JP, Stienen GJM (1996) ATPase activity and force production in skinned rat cardiac muscle under isometric and dynamic conditions. J Mol Cell Cardiol 28:1747-1757

Ebus JP, Stienen GJ, Elzinga G (1994) Influence of phosphate and pH on myofibrillar ATPase activity and force in skinned cardiac trabeculae from rat. J Physiol 476:501-516

Edman KAP, Månsson A, Caputo C (1997) The biphasic force–velocity relationship in frog muscle fibres and its evaluation in terms of cross-bridge function. J Physiol 503:141-156

Ferenczi MA, Bershitsky SY, Koubassova N, Siththanandan V, Helsby WI, Panine P, Roessle M, Narayanan T, Tsaturyan AK (2005) The “roll and lock” mechanism of force generation in muscle. Structure 13:131-141

Ford LE (1991) Mechanical manifestations of activation in cardiac muscle. Circ Res 68:621-637

Ford LE, Huxley AF, Simmons RM (1977) Tension responses to sudden length change in stimulated frog muscle fibres near slack length. J Physiol 269:441-515

Geeves MA, Goody RS, Gutfreund H (1984) Kinetics of acto-S1 interaction as a guide to a model for the crossbridge cycle. J Muscle Res Cell Motil 5:351-361

Geeves MA, Holmes KC (1999) Structural mechanism of muscle contraction. Annu Rev Biochem 68:687-728

Gibbs CL (1978) Cardiac energetics. Physiol Rev 58:174-254

Goldman YE, Brenner B (1987) Special topic: molecular mechanism of muscle contraction. Annu Rev Physiol 49:629-636

Grandi E, Pasqualini FS, Bers DM (2010) A novel computational model of the human ventricular action potential and Ca transient. J Mol Cell Cardiol 48:112-121

Gwathmey JK, Hajjar RJ (1990) Relation between steady-state force and intracellular [Ca^{2+}] in intact human myocardium. Index of myofibrillar responsiveness to Ca^{2+}. Circulation 82:1266-1278

Han JC, Taberner AJ, Tran K, Goo S, Nickerson DP, Nash MO, Nielsen PMF, Crampin EJ, Loiselle DS (2012) Comparison of Gibbs and Suga formulations of cardiac energetics: the demise of "isoefficiency". J Appl Physiol 113:996-1003

Himeno Y, Asakura K, Cha CY, Memida H, Powell T, Amano A, Noma A (2015) A human ventricular myocyte model with a refined representation of excitation-contraction coupling. Biophys J 109:415-427

Hinch R, Greenstein JL, Tanskanen AJ, Xu L, Winslow RL (2004) A simplified local control model of calcium-induced calcium release in cardiac ventricular myocytes. Biophys J 87:3723-3736

Hooijman P, Stewart MA, Cooke R (2011) A new state of cardiac myosin with very slow ATP turnover: a potential cardioprotective mechanism in the heart. Biophys J 100:1969-1976

Hunter PJ, McCulloch AD, Ter Keurs HEDJ (1998) Modelling the mechanical properties of cardiac muscle. Prog Biophys Mol Biol 69:289-331

Huxley AF (1957) Muscle structure and theories of contraction. Prog Biophys Biophys Chem 7:255-318

Huxley AF (1974) Muscular contraction. J Physiol 243:1-43

Huxley AF, Simmons RM (1971) Proposed mechanism of force generation in striated muscle. Nature 233:533-538

Izakov VY, Katsnelson LB, Blyakhman FA, Markhasin VS, Shklyar TF (1991) Cooperative effects due to calcium binding by troponin and their consequences for contraction and relaxation of cardiac muscle under various conditions of mechanical loading. Circ Res 69:1171-1184

Jafri MS, Rice JJ, Winslow RL (1998) Cardiac Ca^{2+} dynamics: the roles of ryanodine receptor adaptation and sarcoplasmic reticulum load. Biophys J 74:1149-1168

Janssen PM, Stull LB, Marban E (2002) Myofilament properties comprise the rate-limiting step for cardiac relaxation at body temperature in the rat. Am J Physiol Heart Circ Physiol 282:H499–507

Kentish JC (1986) The effects of inorganic phosphate and creatine phosphate on force production in skinned muscles from rat ventricle. J Physiol 370:585-604

Kentish JC, Stienen GJ (1994) Differential effects of length on maximum force production and myofibrillar ATPase activity in rat skinned cardiac muscle. J Physiol 475:175-184

Kuhn HJ, Bletz C, Rüegg JC (1990) Stretch-induced increase in the Ca^{2+} sensitivity of myofibrillar ATPase activity in skinned fibres from pig ventricles. Pflugers Arch 415:741-746

Lab MJ, Allen DG, Orchard CH (1984) The effects of shortening on myoplasmic calcium concentration and on the action potential in mammalian ventricular muscle. Circ Res 55:825-829

Landesberg A, Sideman S (1994) Mechanical regulation of cardiac muscle by coupling calcium kinetics with cross-bridge cycling: a dynamic model. Am J Physiol Heart Circ Physiol 267:H779-H795

Lascano EC, Said M, Vittone L, Mattiazzi A, Mundiña-Weilenmann C, Negroni JA (2013) Role of CaMKII in post acidosis arrhythmias: a simulation study using a human myocyte model. J Mol Cell Cardiol 60:172-183

Lombardi V, Piazzesi G (1990) The contractile response during steady lengthening of stimulated frog muscle fibres. J Physiol 431:141-171

Lymn RW, Taylor EW (1971) Mechanism of adenosine triphosphate hydrolysis by actomyosin. Biochemistry 10:4617-4624

Månsson A (2010) Actomyosin-ADP states, interhead cooperativity, and the force-velocity relation of skeletal muscle. Biophys J 98:1237-1246

Månsson A, Rassier D, Tsiavaliaris G (2015) Poorly understood aspects of striated muscle contraction. Biomed Res Int. doi:10.1155/2015/245154

Matsuoka S, Sarai N, Jo H, Noma A (2004) Simulation of ATP metabolism in cardiac excitation–contraction coupling. Prog Biophys Mol Biol 85:279-299

Matsuoka S, Sarai N, Kuratomi S, Ono K, Noma A (2003) Role of individual ionic current systems in ventricular cells hypothesized by a model study. Jpn J Physiol 53:105-123

Moriarty TF (1980) The law of Laplace. Its limitation as a relation for diastolic pressure, volume, or wall stress of the left ventricle. Circ Res 46:321-331

Murakami U, Uchida K (1985) Contents of myofibrillar proteins in cardiac, skeletal, and smooth muscles. J Biochem 98:187-197

Negroni JA, Lascano EC (1996) A cardiac muscle model relating sarcomere dynamics to calcium kinetics. J Mol Cell Cardiol 28:915-929

Negroni JA, Lascano EC (2008) Simulation of steady state and transient cardiac muscle response experiments with a Huxley-based contraction model. J Mol Cell Cardiol 45:300-312

Negroni JA, Morotti S, Lascano EC, Gomes AV, Grandi E, Puglisi JL, Bers DM (2015) β-adrenergic effects on cardiac myofilaments and contraction in an integrated rabbit ventricular myocyte model. J Mol Cell Cardiol 81:162-175

O′Hara T, Virág L, Varró A, Rudy Y (2011) Simulation of the undiseased human cardiac ventricular action potential: model formulation and experimental validation. PloS Comput Biol 7:e1002061

Okada JI, Sugiura S, Nishimura S, Hisada T (2005) Three-dimensional simulation of calcium waves and contraction in cardiomyocytes using the finite element method. Am J Physiol Cell Physiol 288:C510-C522

Peterson JN, Hunter WC, Berman MR (1991) Estimated time course of Ca^{2+} bound to troponin C during relaxation in isolated cardiac muscle. Am J Physiol Heart Circ Physiol 260:H1013-H1024

Piazzesi G, Francini F, Linari M, Lombardi V (1992) Tension transients during steady lengthening of tetanized muscle fibres of the frog. J Physiol 445:659-711

Piazzesi G, Lombardi V (1995) A cross-bridge model that is able to explain mechanical and energetic properties of shortening muscle. Biophys J 68:1966-1979

Potter JD (1974) The content of troponin, tropomyosin, actin, and myosin in rabbit skeletal muscle myofibrils. Arch Biochem Biophys 162:436-441

Rayment I, Holden HM, Whittaker M, Yohn CB, Lorenz M, Holmes KC, Milligan RA (1993) Structure of the actin-myosin complex and its implications for muscle contraction. Science 261:58-65

Rice JJ, Stolovitzky G, Tu Y, de Tombe PP (2003) Ising model of cardiac thin filament activation with nearest-neighbor cooperative interactions. Biophys J 84:897-909

Schramm M, Klieber HG, Daut J (1994) The energy expenditure of actomyosin-ATPase, Ca^{2+}-ATPase and Na^{+}, K^{+}-ATPase in guinea-pig cardiac ventricular muscle. J Physiol 481:647-662

Shim EB, Amano A, Takahata T, Shimayoshi T, Noma A (2007) The cross-bridge dynamics during ventricular contraction predicted by coupling the cardiac cell model with a circulation model. J Physiol Sci 57:275-285

Shim EB, Jun HM, Leem CH, Matusuoka S, Noma A (2008) A new integrated method for analyzing heart mechanics using a cell-hemodynamics-autonomic nerve control coupled model of the cardiovascular system. Prog Biophys Mol Biol 96:44-59

Shimizu H, Fujita T, Ishiwata SI (1992) Regulation of tension development by MgADP and Pi without Ca^{2+}. Role in spontaneous tension oscillation of skeletal muscle. Biophys J 61:1087-1098

Siemankowski RF, White HD (1984) Kinetics of the interaction between actin, ADP, and cardiac myosin-S1. J Biol Chem 259:5045-5053

Siemankowski RF, Wiseman MO, White HD (1985) ADP dissociation from actomyosin subfragment 1 is sufficiently slow to limit the unloaded shortening velocity in vertebrate muscle. Proc Natl Acad Sci USA 82:658-662

Sipido KR, Wier WG (1991) Flux of Ca^{2+} across the sarcoplasmic reticulum of guinea-pig cardiac cells during excitation-contraction coupling. J Physiol 435:605-630

Smith DA, Geeves MA, Sleep J, Mijailovich SM (2008) Towards a unified theory of muscle contraction. I: foundations. Ann Biomed Eng 36:1624-1640

Soltis AR, Saucerman JJ (2010) Synergy between CaMKII substrates and β-adrenergic signaling in regulation of cardiac myocyte Ca^{2+} handling. Biophys J 99:2038-2047

Spudich JA (1994) How molecular motors work. Nature 372:515-518

Stehle R, Iorga B (2010) Kinetics of cardiac sarcomere processes and rate-limiting steps in contraction and relaxation. J Mol Cell Cardiol 48:843-850

Stienen GJ, Kiers JL, Bottinelli R, Reggiani C (1996) Myofibrillar ATPase activity in skinned human skeletal muscle fibres: fibre type and temperature dependence. J Physiol 493:299-307

Suga H (1990) Ventricular energetics. Physiol Rev 70:247-277

Sugi H, Minoda H, Inayoshi Y, Yumoto F, Miyakawa T, Miyauchi Y, Tanokura M, Akimoto T, Kobayashi T, Chaen S, Sugiura S (2008) Direct demonstration of the cross-bridge recovery stroke in muscle thick filaments in aqueous solution by using the hydration chamber. Proc Natl Acad Sci USA 105:17396-17401

Trentham DR, Eccleston JF, Bagshaw CR (1976) Kinetic analysis of ATPase mechanisms. Q Rev Biophys 9:217-281

Utaki H, Taniguchi K, Konishi H, Himeno Y, Amano A (2016) A Method for Determining Scale Parameters in a Hemodynamic model incorporating Cardiac Cellular Contraction model. Adv Biomed Eng 5:32-42

Wannenburg T, Janssen PM, Fan D, de Tombe PP (1997) The Frank-Starling mechanism is not mediated by changes in rate of cross-bridge detachment. Am J Physiol Heart Circ Physiol 273:H2428-H2435

Widén C, Barclay CJ (2006) ATP splitting by half the cross-bridges can explain the twitch energetics of mouse papillary muscle. J Physiol 573:5-15

Woledge RC (1998) Techniques for muscle energetics. *In* Current methods in muscle physiology, Sugi H (ed), Oxford University Press, New York, NY, pp.343-370

Wu S, Liu J, Reedy MC, Tregear RT, Winkler H, Franzini-Armstrong C, Sasaki H, Lucaveche C, Goldman YE, Reedy MK, Taylor KA (2010) Electron tomography of cryofixed, isometrically contracting insect flight muscle reveals novel actin-myosin interactions. PloS One 5:e12643

Yount RG, Lawson D, Rayment I (1995) Is myosin a" back door" enzyme?. Biophys J 68:44S-49S

Yue DT, Marban E, Wier WG (1986) Relationship between force and intracellular [Ca^{2+}] in tetanized mammalian heart muscle. J Gen Physiol 87:223–42

Chapter 3: Mitochondria in cardiomyocyte; Diseases & Diagnosis

3.1 Mitochondria in cardiomyocytes

Mitochondria play the important role as the energy producer for cardiomyocytes. The mitochondria of adult cardiomyocytes produce 90% of ATP via electron transport chain (*see* Chapter 1). However, heart requires rhythmic contraction of pump throughout the life. The tight coupling between mitochondria and ATP consumption which mainly from cardiac contraction (*see* Chapter 2), requires the optimized cellular organization. The malfunction of mitochondria could impair cell energetics leading to heart failure causing reduced ATP production, increased reactive oxygen species production, and aberrant apoptotic induction (Tuppen et al. 2010). Due to the mutations, there is the accumulation in the number of mitochondrial DNA (mtDNA) before the symptoms occurred. In addition, mitochondrial genetics are non-Mendelian genetics in following ways (Figure 3-1): 1) Maternal inheritance; mtDNA is strictly inherited from mother, 2) Heteroplasmy; normally mtDNA are identical. When the mutations are occurred at the beginning, it affects some but not all (wild type + mutant called 'heteroplasmy'), 3) Mitotic segregation; there is the random distribution of organelles at the time of cell division, and 4) Threshold effect; the clinical phenotype is determined by the relative proportion between wild type and mutant mitochondrial molecules. Threshold expression is usually 50%-100% mutant mtDNA that determines the disease stage.

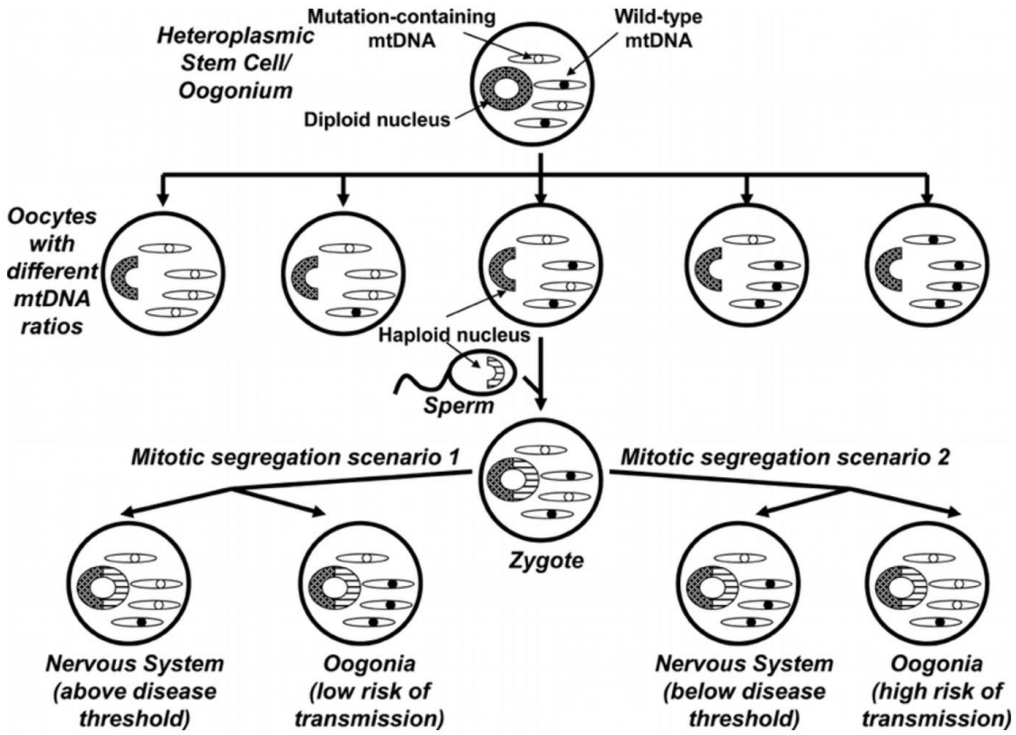

Figure 3-1 Maternal inheritance, heteroplasmy, mitotic segregation, and threshold effects distinguish mitochondrial genetics from Mendelian genetics.

Source Swerdlow 2011

3.2 Mitochondrial diseases

Mitochondrial diseases are the complex diseases associated to dysfunction or failures of the mitochondria (the changes in ATP production) and they are the results of either inherited or spontaneous mutations in mtDNA or nuclear DNA. The ~15% mitochondrial diseases are caused by mutations in mtDNA (acquired or inherited). However, there are a variety in the symptoms and any organs can be affected, especially in organ with high energy demands (high number of mitochondria), e.g., heart, brain, muscles, and endocrine system.

Mitochondrial cardiomyopathy is described by abnormal heart-muscle structure and/or function, secondary to genetic defects involving the electron transport chain, in the absent of concomitant coronary artery disease, hypertension, valvular disease, or congenital heart disease. The typical cardiac diseases associated to mitochondrial diseases are including hypertrophic and dilated cardiomyopathy, arrhythmias, left ventricular myocardial noncompaction, and heart failure (Holmgren et al. 2003, Debray et al. 2007, Meyers et al. 2013). Nevertheless, mitochondrial cardiomyopathy often shows clinically expression by multisystemic diseases described below. (Meyers et al. 2013).

- *Cardiovascular system* [heart failure, arrhythmias, murmurs, sudden death, left ventricular myocardial noncompaction, apical ballooning syndrome]
- *Pulmonary system* [dyspnea, orthopnea, respiratory failure, respiratory acidosis]
- Neurological system [encephalopathy, ataxia, movement disorders, seizure disorders, mental retardation]
- *Renal system* [renal failure, benign renal cysts, focal segmental glomerulosclerosis, proximal tubulopathy, nephritic syndrome, tubulointerstitial nephritis]
- *Hematological system* [anemia, leukopenia, thrombocytopenia, eosinophilia]
- *Endocrine system* [diabetes mellitus, diabetes insipidus, hypothyroidism, hypoparathyroidism, adrenocorticotropic hormone deficiency, hypogonadism, amenorrhea, gynecomastia]
- *Musculoskeletal system* [muscle weakness with normal creatine kinase levels and normal electromyographic and nerve-conduction studies, short stature, microcephaly, round face, high forehead, low-set ears, short neck]
- *Skin and soft tissue* [hypertrichosis, eczema, vitiligo, multiple lipomatosis, reticular pigmentation]
- *Gastrointestinal system* [periodontosis, anorexia, abdominal pain, nausea, vomiting, diarrhea, malabsorption, villous atrophy, constipation, pseudo-obstruction, pancreatitis, elevated liver enzyme levels]
- *Ophthalmic system* [external ophthalmoparesis, retinitis pigmentosa]
- *Auditory system* [sensorineural hearing loss]

On the other hand, some mitochondrial syndromes are associated to cardiovascular manifestation (Meyers et al. 2013) such as;

- *Dilated cardiomyopathy and left ventricular hypertrabeculation* [Barth syndrome (lethal infantile cardiomyopathy) and Mitochondrial encephalopathy, lactic acidosis, and stroke-like episodes]
- *Arrhythmia* [Chronic progressive external ophthalmoplegia and Kearns-Sayre syndrome]
- *Cardiomyopathy* [Neurogenic muscle weakness, ataxia, and retinitis pigmentosa, and Maternally inherited Leigh syndrome]
- *Cardiomyopathy and arrhythmia* [Leigh syndrome (subacute necrotizing encephalomyelopathy), and Myoclonic epilepsy and ragged red fibers]
- *Left ventricular hypertrabeculation and arrhythmia* [Maternally inherited diabetes and deafness]

3.2.1 DNA mutations related to mitochondrial diseases

Current knowledge reveals that mitochondrial diseases can results from mutations in either the mtDNA or nuclear DNA (Table 3-1).

Table 3-1 The pathophysiology of mitochondrial disorders from DNA mutations.

Complex*	Nuclear DNA mutations	Mitochondrial DNA mutations
I	Leigh syndrome	Leber hereditary optic neuropathy
	Leukodystrophy	Mitochondrial encephalomyopathy, lactic acidosis, and stroke-like episodes
II	Leigh syndrome	-
	Paraganglioma	
	Pheochromocytoma	
III	Leigh syndrome	Cardiomyopathy
	Growth retardation, aminoaciduria, lactic acidosis, and early death	Encephalomyopathy
	Leigh syndrome	Sporadic anemia
IV	Cardioencephalomyopathy	Myopathy
	-	Amyotropic lateral sclerosis-like syndrome
V		Neuropathy, ataxia, and retinitis pigmentosa
		Maternally inherited Leigh syndrome
		Familial bilateral striatal necrosis

**see* Figure 1-3

Source Meyers et al. 2013

The mtDNA mutations are frequently found in 1 of every 200 samples of core blood (Elliott et al. 2010, Chinnery et al. 2012). In pathological state, however, mutations are commonly observed (Fabrizi et al. 1996, Choi et al. 2008) since the mutation rates of mtDNA are 10 times higher than in nuclear DNA. Over 50 pathogenic mtDNA based substitution mutations such as single deletions, one to several point-mutations have been identified. The mtDNA has a very high mutation rate and described in a mixture of wild-type and mutant mtDNA.

Mitochondrial mutations are the typical cause of left ventricular myocardial noncompaction, which is also known as left ventricular hypertrabeculation, characterized by prominent ventricular trabeculations and deep recesses that extend from the left ventricular cavity to subendocardial surface of the ventricular (Stollberger et al. 2002, Jenni et al. 2001, 2007).

3.2.2 Mutations in cytochrome *b* gene of mtDNA

Missense mutations in mtDNA, particularly in cytochrome *b* gene sequences in complex III located at position 14,747-15,887 on the mitochondrial genome have been associated with several diseases with cardiac and muscle involvement described in Table 3-2.

Moreover, hypertrophic cardiomyopathy have been associated with the mutations in mitochondrial cytochrome *b* gene (Valnot et al. 1999, Andreu et al. 2000, Hagen et al. 2013) e.g., 14751 C>T (Hinttala et al. 2006), 14813 A>G (Behar et al. 2008), 14927 A>G (Obayashi et al. 1992, Marin-Garcia et al. 2000, Casademont & Miro 2002), 15024 G>A (Tang et al. 2010a), 15257 G>A (Rose et al. 2001), 15287 T>C (Ballana et al. 2008), 15315 C>T (Fraumene et al. 2006), 15452 C>A (Marin-Garcia & Goldenthal 1997), 15482 T>C, and 15813 T>C (Behar et al. 2008).

Table 3-2 Mutations in mitochondrial cytochrome *b* gene sequence associated with muscle diseases.

Position	Nucleotide substitution	Amino acid substitution*	Diseases	References
14846	G > A	G > S	Exercise intolerance	Andreu et al. 1999b, Taivassalo et al. 2001, 2002, Filosto et al. 2003, Pereira et al. 2011
14849	T > C	S > P	Exercise intolerance	Schuelke et al. 2002, Massie et al. 2010, Pereira et al. 2011
15059	G > A	G > Ter	Mitochondrial myopathy	Andreu et al. 1999a,1999b
15084	G > A	W > Ter	Exercise intolerance	Andreu et al. 1999b, Filosto et al. 2003
15150	G > A	W > Ter	Exercise intolerance	Legros et al. 2001
15168	G > A	W > Ter	Exercise intolerance	Andreu et al. 1999b, Filosto et al. 2003
15170	G > A	G > Ter	Exercise intolerance	Bruno et al. 2003
15197	T > C	S > P	Exercise intolerance	Legros et al. 2001, Pereira et al. 2011
15243	G > A	G > E	Hypertrophic cardiomyopathy	Valnot et al. 1999, Nishigaki et al. 2010, Bannwarth et al. 2013
15497	G > A	G > S	Exercise intolerance	Okura et al. 2003, Tanaka et al. 2004, Tarnopolsky et al. 2004, Pereira et al. 2011
15498	24 base pairs deletion	GDPDNYTL deletion	Exercise intolerance	Andreu et al. 1999b, Taivassalo et al. 2001
15579	A > G	Y > C	Exercise intolerance	Wibrand et al. 2001, Pereira et al. 2011, Ghelli et al. 2013, Krag et al. 2013
15615	G > A	G > D	Exercise intolerance	Bouzidi et al. 1996, Dumoulin et al. 1996, Pereira et al. 2011
15649	18 base pairs deletion	ILAMIP deletion	Exercise intolerance	Carossa et al. 2014

Table 3-2 (continued)

Position	Nucleotide substitution	Amino acid substitution*	Diseases	References
15693	T > C	M > T	Possibly left ventricular noncompaction cardiomyopathy-associated	Tang et al. 2010
15699	G > C	R > P	Muscle weakness	Blakely et al. 2005, Bannwarth et al. 2013
15723	G > A	W > Ter	Exercise intolerance	Andreu et al. 1999b
15761	G > A	G > Ter	Mitochondrial myopathy	Mancuso et al. 2003
15762	G > A	G > E	Mitochondrial myopathy	Andreu et al. 1998
15800	C > T	Q > Ter	Exercise intolerance / Myopathy	Lamantea et al. 2002, Valente et al. 2009

*amino acid abbreviation; one letter code (below) and Ter = Termination or stop codon

A	Alanine	R	Arginine	N	Asparagine
D	Aspartic acid	C	Cysteine	E	Glutamic acid
Q	Glutamine	G	Glycine	H	Histidine
I	Isoleucine	L	Leucine	K	Lysine
M	Methionine	F	Phenylalanine	P	Proline
S	Serine	T	Threonine	W	Tryptophan
Y	Tyrosine	V	Valine		

3.3 Diagnosis of mitochondrial diseases

Routinely, the muscle biopsy is the gold standard for the diagnosis of mitochondrial diseases. However, this technique could observe the structure changes providing the sensitivity and specificity less than 100%. Meyers et al. (2013) summarized several proposed diagnostic criteria that including clinical, histological, enzymological, functional, and molecular factors (Table 3-3).

Table 3-3 Diagnosis criteria for mitochondrial disorders.

Factors	Major diagnosis criteria	Minor diagnostic criteria
Clinical	Mitochondrial syndrome or involvement of any 3 of the following systems: neurologic, muscular, cardiac, renal, nutritional, hepatic, endocrine, hematologic, otologic, ophthalmologic, dermatologic, or dysmorphic; exacerbations; family history of mitochondrial DNA mutations; or exclusion of alternate diagnosis	Symptoms compatible with the respiratory chain defect
Histological	>2% ragged red fibers in skeletal muscle	1%–2% ragged red fibers in patient 30 to 50 years, any ragged red fibers in a patient <30 years, >2% subsarcolemmal mitochondrial accumulations in a patient <16 years, or widespread electron microscopic abnormalities in any tissue
Enzymological	>2% cytochrome *c* oxidase-negative fibers in a patient <50 years, >5% cytochrome *c* oxidase-negative fibers in a patient ≥50 years, <20% activity of any respiratory chain complex in a tissue, <30% activity of any respiratory chain complex in a cell line, or <30% activity of the same respiratory chain complex activity in ≥2 tissues	Antibody-based demonstration of a defect in respiratory chain complex expression, 20%-30% activity of any respiratory chain complex in a tissue, 30%-40% activity of any respiratory chain complex in a cell line, or 30%-40% activity of the same respiratory chain complex activity in ≥2 tissues
Functional	Fibroblast ATP synthesis rates >3 SD units below the mean	Fibroblast ATP synthesis rates 2 to 3 SD units below the mean, or fibroblasts unable to grow on media with glucose replaced by galactose
Molecular	Identification of nuclear DNA or mitochondrial DNA mutation of undisputed pathogenicity	Identification of nuclear DNA or mitochondrial DNA mutation of probable pathogenicity
Metabolic	-	One or more metabolic indicators of impaired respiratory chain function

Source Meyers et al. 2013 (reproduced from Bernier et al. 2002)

3.3.1 Mutations diagnosis using PCR based sequencing

Diagnosis of the mutations using molecular techniques could provide the health monitoring and disease investigating at early stage. Molecular techniques, especially polymerase chain reaction (PCR) and sequencing, are high sensitivity and specificity and useful for early stage detection.

Up to date, the new generation sequencing shows the capability to sequence whole mitochondrial genomes at high coverage of over 1000-fold, which provides sufficient depth to identify the mutation at even low levels (Zaragoza et al. 2010, Goto et al. 2011). Although the advantages of using such technology are clear, and can detect the mutations which are interpreted as being true mutations but are erroneous (Loman et al. 2012).

We designed the universal primers for detecting the mutations located at the conserved sequence of mitochondrial cytochrome *b* gene (Table 3-4). These novel primers could be the merit for human and wide range of experimental animals to observe the mutations in cytochrome *b* gene of mtDNA. The mutation results will notice by observing the double peak on sanger sequence chromatograms (Figure 3-2). The alignment of human mtDNA with novel primers from Muangkram et al. (2016) was illustrated in Figure 3-3.

Table 3-4 Universal primers for mutations diagnosis.

Primers	Sequences	Position*	Annealing temperature
Forward primer	5′-TTY GCA TAC GCA ATC YTA CGA TC-3′	15572-15594	55ºC
Reverse primer	5′-GTT GKC CTC CRA TTC ATG TRA G-3′	15749-15770	

*The position on mitochondrial DNA based on human mitochondrial genome (GenBank number V00662.1; Anderson et al. 1981).

Source Muangkram et al. 2016

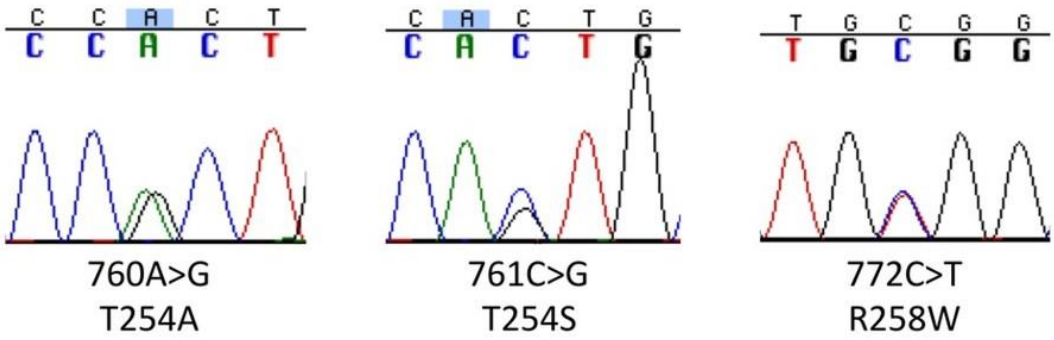

Figure 3-2 Double peak of missense mutations from sanger sequence chromatograms.

Source Izumi et al. 2015

Five mutations in cytochrome *b* gene of mtDNA located at position 15595-15749 of human mitochondrial genome could be diagnosed by using the novel primers (Figure 3-3).

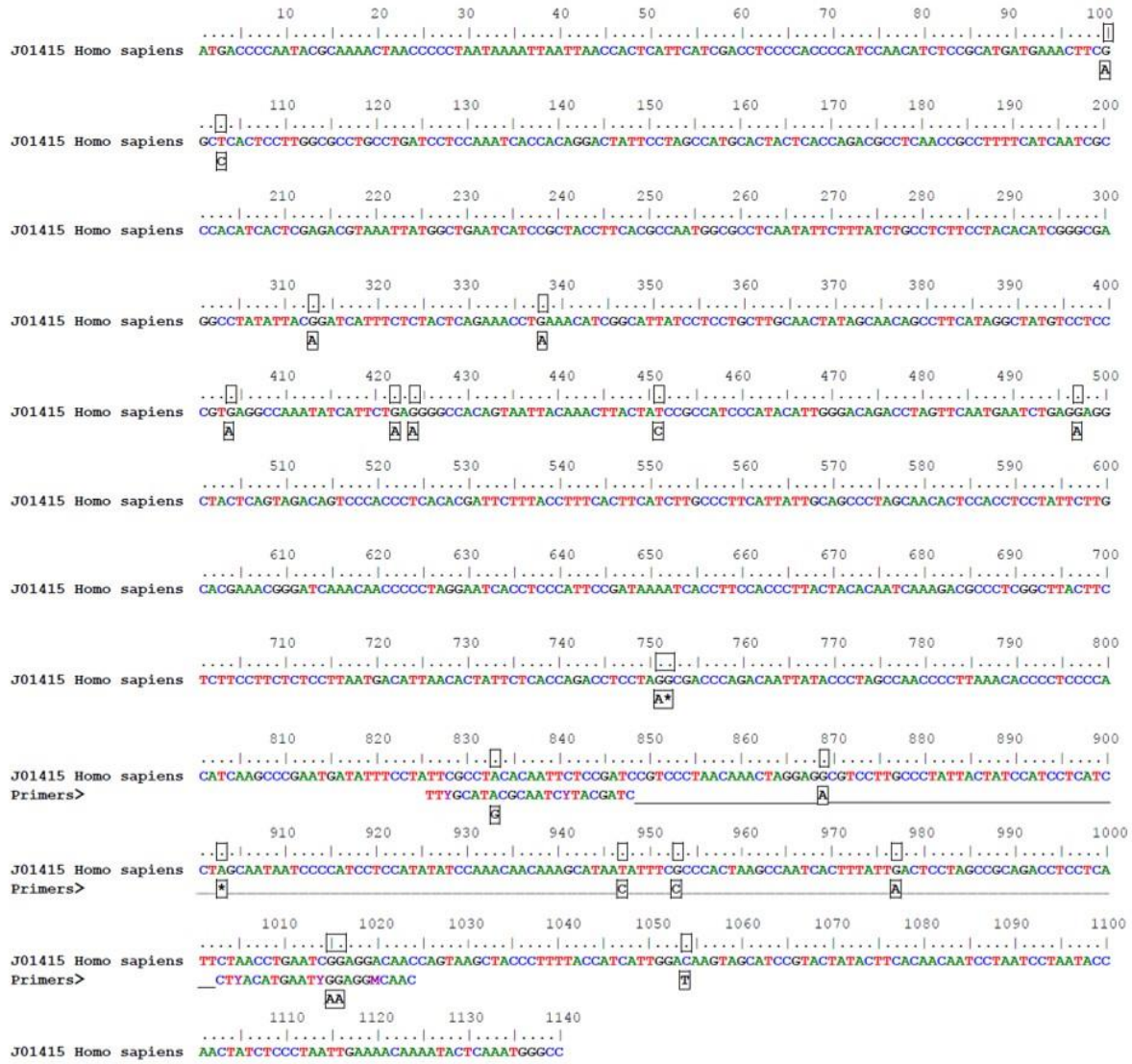

Figure 3-3 The alignment of human mitochondrial cytochrome *b* gene sequence with new primers. Primers could amplify the fragment of mitochondrial cytochrome *b* gene sequence sized 154 base pairs in length (PCR product sized 199 base pairs in length) with the ability to investigate the mutations 5 positions (25%). The '.' refers to the mutation position related with muscle diseases from Table 3-2 and the letter in square refer to the nucleotide changes. The '*' indicates the first base of deletion mutations. The baseline of these sequences corresponds to position number 14747 of complete human mitochondrial genome (J01415.2; Anderson et al. 1981).

3.3.2 The application in high resolution melt analysis

High resolution melt (HRM) analysis is the useful tool for investigating the single nucleotide polymorphism. This technique could eliminate the errors which may come from the sequencing reactions or long PCR amplification (Elliott et al. 2012, Lloyd et al. 2012). HRM technique provides the high sensitivity level as reported in wide studies (Figure 3-4). However, the limitation of HRM technique is the DNA fragment should less than 200 base pairs. The implication of novel primers with HRM could serve as useful tool to detect the mutations at early stage.

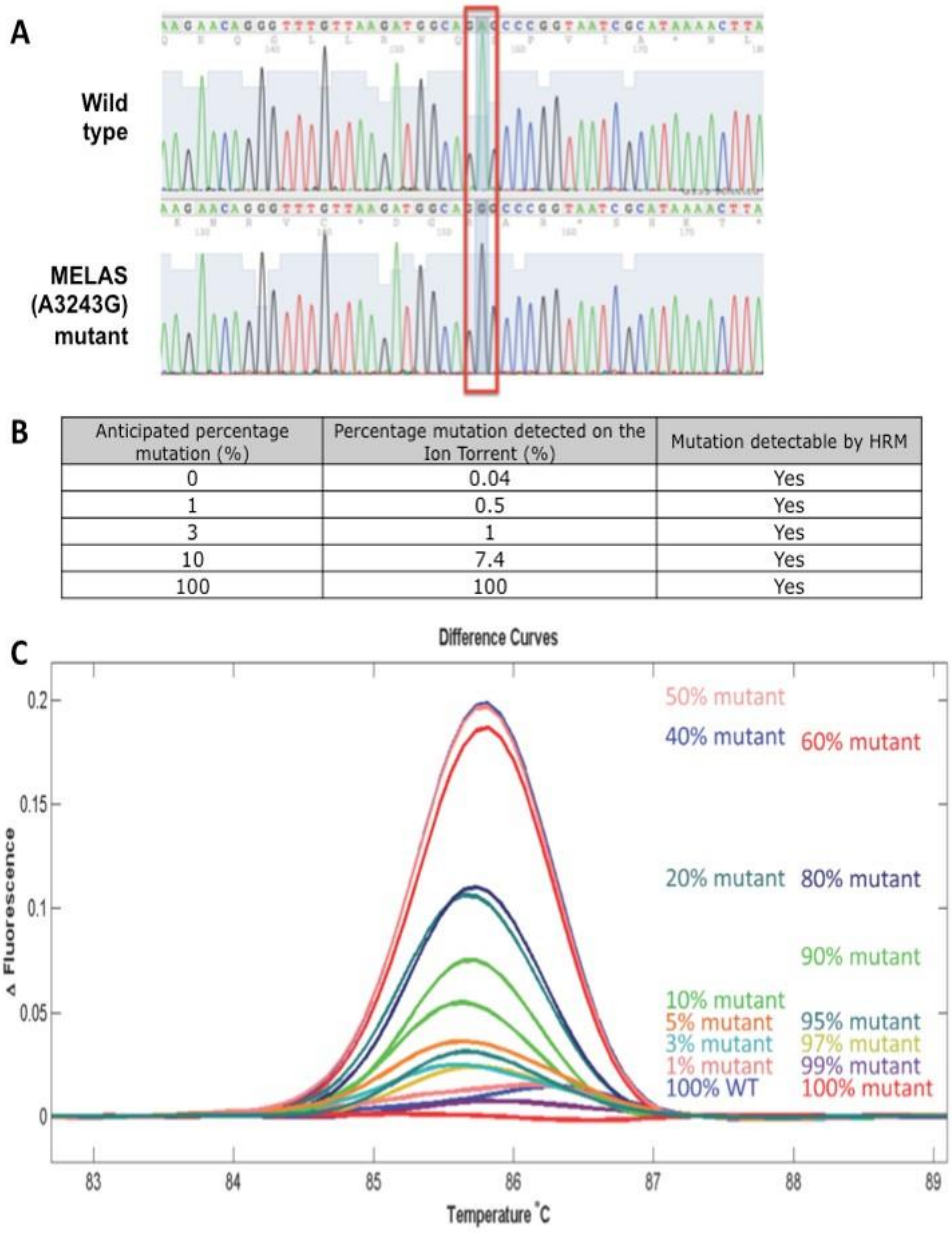

Anticipated percentage mutation (%)	Percentage mutation detected on the Ion Torrent (%)	Mutation detectable by HRM
0	0.04	Yes
1	0.5	Yes
3	1	Yes
10	7.4	Yes
100	100	Yes

Figure 3-4 Application of high resolution melt analysis.

Panel A; Capillary sequencing between wild type and mutation, Panel B; Sensitivity level of ion torrent to detect specific percentage of mutation (mixed sample), Panel C; The results of HRM

Source Yeung et al. 2014

3.4 References

Anderson S, Bankier AT, Barrell BG, de Bruijn MH, Coulson AR, Drouin J, Eperon IC, Nierlich DP, Roe BA, Sanger F, Schreier PH, Smith AJ, Staden R, Young IG (1981) Sequence and organization of human mitochondrial genome. Nature 290:457-465

Andreu AL, Bruno C, Dunne TC, Tanji K, Shanske S, Sue CM, Krishna S, Hadjigeorgiou GM, Shtilbans A, Bonilla E, DiMauro S (1999a) A nonsense mutation (G15059A) in the cytochrome *b* gene in a patient with exercise intolerance and myoglobinuria. Ann Neurol 45:127-130

Andreu AL, Bruno C, Shanske S, Shtilbans A, Hirano M, Krishna S, Hayward L, Systrom DS, Brown RH, DPhil Jr, DiMauro S (1998) Missense mutation in the mtDNA cytochrome *b* gene in a patient with myopathy. Neurology 51:1444-1447

Andreu AL, Checcarelli N, Iwata S, Shanske S, DiMauro S (2000) A missense mutation in the mitochondrial cytochrome *b* gene in a revisited case with histiocytoid cardiomyopathy. Pediatr Res 48:311-314

Andreu AL, Hanna MG, Reichmann H, Bruno C, Penn AS, Tanji K, Pallotti F, Iwata S, Bonilla E, Lach B, Morgan-Hughes J, Shanske S, Sue CM, Pulkes T, Siddiqui A, Clark JB, Land J, Iwata M, Schaefer J, DiMauro S (1999b) Exercise intolerance dur to mutations in the cytochrome *b* gene of mitochondrial DNA. N Engl J Med 341:1037-1044

Ballana E, Govea N, de Cid R, Garcia C, Arribas C, Rosell J, Estivill X (2008) Detection of unrecognized low‐level mtDNA heteroplasmy may explain the variable phenotypic expressivity of apparently homoplasmic mtDNA mutations. Hum Mutat 29:248-257

Bannwarth S, Procaccio V, Lebre AS, Jardel C, Chaussenot A, Hoarau C, Maoulida H, Charrier N, Gai X, Xie HM, Ferre M, Fragaki K, Hardy G, de Camaret BM, Marlin S, Dhaenens CM, Slama A, Rocher C, Bonnefont JP, Rötig A, Aoutil N, Gilleron M, Desquiret-Dumas V, Reynier P, Ceresuela J, Jonard L, Devos A, Espil-Taris C, Martinez D, Gaignard P, Le Quan Sang KH, Amati-Bonneau P, Falk MJ, Florentz C, Chabrol B, Durand-Zaleski I, Paquis-Flucklinger V (2013) Prevalence of rare mitochondrial DNA mutations in mitochondrial disorders. J Med Genet 50:704-714

Behar DM, Villems R, Soodyall H, Blue-Smith J, Pereira L, Metspalu E, Scozzari R, Makkan H, Tzur S, Comas D, Bertranpetit J, Quintana-Murci L, Tyler-Smith C, Wells RS, Rosset S, The Genographic Consortium (2008) The dawn of human matrilineal diversity. Am J Hum Genet 82:1130–1140

Bernier FP, Boneh A, Dennett X, Chow CW, Cleary MA, Thorburn DR (2002) Diagnostic criteria for respiratory chain disorders in adults and children. Neurology 59:1406-1411

Blakely EL, Mitchell AL, Fisher N, Meunier B, Nijtmans LG, Schaefer AM, Jackson MJ, Turnbull DM, Taylor RW (2005) A mitochondrial cytochrome *b* mutation causing severe respiratory chain enzyme deficiency in humans and yeast. Febs J 272:3583-3592

Bouzidi MF, Carrier H, Godinot C (1996) Antimycin resistance and ubiquinol cytochrome *c* reductase instability associated with a human cytochrome *b* mutation. Biochim Biophys Acta 1317:199-209

Bruno C, Santorelli FM, Assereto S, Tonoli E, Tessa A, Traverso M, Scapolan S, Bado M, Tedeschi S, Minetti C (2003) Progressive exercise intolerance associated with a new muscle-restricted nonsense mutation (G142X) in the mitochondrial cytochrome *b* gene. Muscle Nerve 28:508-511

Carossa V, Ghelli A, Tropeano CV, Valentino ML, Iommarini L, Maresca A, Caporali L, la Morgia C, Liguori R, Barboni P, Carbonelli M, Rizzo G, Tonon C, Lodi R, Martinuzzi A, de Nardo V, Rugolo M, Ferretti L, Gandini F, Pala M, Achilli A, Olivieri A, Torroni A, Carelli V (2014) A novel in-frame 18-bp microdeletion in *MT-CYB* causes a multisystem disorder with prominent exercise intolerance. Hum Mutat 35:954-958

Casademont J, Miro O (2002) Electron transport chain defects in heart failure. Heart Fail Rev 7:131–139

Chinnery PF, Elliott HR, Hudson G, Samuels DC, Relton CL (2012) Epigenetics, epidemiology and mitochondrial DNA diseases. Int J Epidemiol 41:177-187

Christodoulou DrJ, McInnes RR, Jay V, Wilson G, Becker LE, Lehotay DC, Platt BA, Bridge PJ, Robinson BH, Clarke JTR (1994) Barth syndrome: clinical observations and genetic linkage studies. Am J Med Genet 50:255-264

Choi BO, Hwang JH, Kim J, Cho EM, Cho SY, Hwang SJ, Lee HW, Kim SJ, Chung KW (2008) A MELAS syndrome family harboring two mutations in mitochondrial genome. Exp Mol Med 2:354-360

Debray FG, Lambert M, Chevalier I, Robitaille Y, Decarie JC, Shoubridge EA, Robinson BH, Mitchell GA (2007) Long-term outcome and clinical spectrum of 73 pediatric patients with mitochondrial diseases. Pediatrics 119:722-733

Dumoulin R, Sagnol I, Ferlin T, Bozon D, Stepien G, Mousson B (1996) A novel gly290asp mitochondrial cytochrome *b* mutation linked to a complex III deficiency in progressive exercise intolerance. Mol Cell Probes 10:389-391

Elliott AM, Radecki J, Moghis B, Li X, Kammesheidt A (2012) Rapid detection of the ACMG/ACOG-recommended 23 CFTR disease-causing mutations using ion torrent semiconductor sequencing. J Biomol Tech 2:24-30

Elliott HR, Samuels DC, Eden JA, Relton CL, Chinnery PF (2008) Pathogenic mitochondrial DNA mutations are common in the general population. Am J Hum Genet 83:254-260

Fabrizi GM, Cardaioli E, Grieco GS, Cavallaro T, Malandrini A, Manneschi L, Dotti MT, Federico A, Guazzi G (1996) The A to G transition at nt 3243 of the mitochondrial $tRNA^{Leu(UUR)}$ may cause an MERRF syndrome. J Neurol Neurosurg Psychiatry 2:47-51

Filosto M, Mancuso M, Vives-Bauza C, Vilà MR, Shanske S, Hirano M, Andreu AL, DiMauro S (2003) Lack of paternal inheritance of muscle mitochondrial DNA in sporadic mitochondrial myopathies. Ann Neurol 54:524-526

Fraumene C, Belle EMS, Castrì L, Sanna S, Mancosu G, Cosso M, Marras F, Barbujani G, Pirastu, Angius A (2006) High resolution analysis and phylogenetic network construction using complete mtDNA sequences in Sardinian genetic isolates. Mol Biol Evol 23:2101-2111

Ghelli A, Tropeano CV, Calvaruso MA, Marchesini A, Iommarini L, Porcelli AM, Zanna C, de Nardo V, Martinuzzi A, Wibrand F, Vissing J, Kurelac I, Gasparre G, Selamoglu N, Daldal F, Rugolo M (2013) The cytochrome *b* p.278Y>C mutation causative of a multisystem disorder enhances superoxide production and alters supramolecular interactions of respiratory chain complexes. Hum Mol Genet 22:2141-2151

Goto H, Dickins B, Afgan E, Paul IM, Taylor J, Makova KD, Nekrutenko A (2011) Dynamics of mitochondrial heteroplasmy in three families investigated via a repeatable re-sequencing study. Genome Biol 2:R59

Hagen CM, Aidt FH, Havndrup O, Hedley PL, Jespersgaard C, Jensen M, Kanters JK, Moolman-Smook JC, Møller DV, Bundgaard H, Christiansen M (2013) *MT-CYB* mutations in hypertrophic cardiomyopathy. Mol Genet Genomic Med 1:54-65

Hinttala R, Smeets R, Moilanen JS, Ugalde C, Uusimaa J, Smeitink JAM, Majamaa K (2006) Analysis of mitochondrial DNA sequences in patients with isolated or combined oxidative phosphorylation system deficiency. J Med Genet 43:881–886

Holmgren D, Wahlander H, Eriksson BO, Oldfors A, Holme E, Tulinius M (2003) Cardiomyopathy in children with mitochondrial disease; clinical course and cardiological findings. Eur Heart J 24:280-288

Izumi K, Nakato R, Zhang Z, Edmondson AC, Noon S, Dulik MC, Rajagopalan R, Venditti CP, Gripp K, Samanich J, Zackai EH, Deardorff MA, Clark D, Allen JL, Dorsett D, Misulovin Z, Komata M, Bando M, Kaur M, Katou Y, Shirahige K, Krantz ID (2015) Germline gain-of-function mutations in *AFF4* cause a developmental syndrome functionally linking the super elongation complex and cohesin. Nat Genet 47:338-344

Jenni R, Oechslin E, Schneider J, Attenhofer Jost C, Kaufmann PA (2001) Echocardiographic and pathoanatomical characteristics of isolated left ventricular non-compaction: a step towards classification as a distinct cardiomyopathy. Heart 86:666-671

Jenni R, Oechslin EN, van der Loo B (2007) Isolated ventricular non-compaction of the myocardium in adults. Heart 93:11-15

Krag TO, Hauerslev S, Jeppesen TD, Duno M, Vissing J (2013) Muscle regeneration in mitochondrial myopathies. Mitochondrion 13:63-70

Lamantea E, Carrara F, Mariotti C, Morandi L, Tiranti V, Zeviani M (2002) A novel nonsense mutation (Q352X) in the mitochondrial cytochrome *b* gene associated with a combined deficiency of complexes I and III. Neuromuscul Disord 12:49-52

Legros F, Chatzoglou E, Frachon P, de Baulny HO, Laforêt P, Jardel C, Godinot C, Lombès A (2001) Functional characterization of novel mutations in the human cytochrome *b* gene. Eur J Hum Genet 9:510-581

Lloyd RE, Foster PG, Guille M, Littlewood DT (2012) Next generation sequencing and comparative analyses of *Xenopus* mitogenomes. BMC Genomics 13:496

Loman NJ, Misra RV, Dallman TJ, Constantinidou C, Gharbia SE, Wain J, Pallen MJ (2012) Performance comparison of benchtop high-throughput sequencing platforms. Nat Biotechnol 30:434-439

Mancuso M, Filosto M, Stevens JC, Patterson M, Shanske S, Krishna S, DiMauro S (2003) Mitochondrial myopathy and complex III deficiency in a patient with a new stop-codon mutation (G339X) in the cytochrome *b* gene. J Neurol Sci 209:61-63

Marin-Garcia J, Ananthakrishnan R, Goldenthal MJ, Pierpont ME (2000) Biochemical and molecular basis for mitochondrial cardiomyopathy in neonates and children. J Inherit Metab Dis 23:625–633

Marin-Garcia J, Goldenthal MJ (1997) Mitochondrial cardiomyopathy: molecular and biochemical analysis. Pediatr Cardiol 18:251–260

Massie R, Wong LJ, Milone M (2010) Exercise intolerance due to cytochrome *b* mutation. Muscle Nerve 42:136-140

Meyers AD, Basha HI, Koenig MK (2013) Mitochondrial cardiomyopathy. Tex Heart Inst J 40:385-394

Muangkram Y, Wajjwalku W, Amano A, Sukmak M (2016) The novel primers for mammal species identification-based mitochondrial cytochrome *b* sequence: implication for reserved wild animals in Thailand and endangered mammal species in Southeast Asia. Mitochondrial DNA A DNA Mapp Seq Anal doi:10.1080/24701394.2016.1238902

Nishigaki Y, Ueno H, Coku J, Koga Y, Fujii T, Sahashi K, Nakano K, Yoneda M, Nonaka M, Tang L, Liou CW, Paquis-Flucklinger V, Harigaya Y, Ibi T, Goto Y, Hosoya H, DiMauro S, Hirano M, Tanaka M (2010) Extensive screening system using suspension array technology to detect mitochondrial DNA point mutations. Mitochondrion 10:300-308

Obayashi T, Hattori K, Sugiyama S, Tanaka M, Tanaka T, Itoyama S, Deguchi H, Kawamura K (1992) Point mutations in mitochondrial DNA in patients with hypertrophic cardiomyopathy. Am Heart J 124:1263-1269

Okura T, Koda M, Ando F, Niino N, Tanaka M, Shimokata H (2003) Association of the mitochondrial DNA 15497G/A polymorphism with obesity in a middle-aged and elderly Japanese population. Hum Genet 113:432-436

Pereira L, Soares P, Radivojac P, Li B, Samuels DC (2011) Comparing phylogeny and the predicted pathogenicity of protein variations reveals equal purifying selection across the global human mtDNA diversity. Am J Hum Genet 88:433-439

Rose G, Passarino G, Carrieri G, Altomare K, Greco V, Bertolini S, Bonafè M, Franceschi C, de Benedictis G (2001) Paradoxes in longevity: sequence analysis of mtDNA haplogroup J in centenarians. Eur J Hum Genet 9:701-707

Schuelke M, Krude H, Finckh B, Mayatepek E, Janssen A, Schmelz M, Trefz F, Trijbels F, Smeitink J (2002) Septo-optic dysplasia associated with a new mitochondrial cytochrome *b* mutation. Ann Neurol 51:388-392

Stollberger C, Finsterer J, Blazek G. (2002) Left ventricular hypertrabeculation / noncompaction and association with additional cardiac abnormalities and neuromuscular disorders. Am J Cardiol 90:899-902

Swerdlow RH (2011) Role and treatment of mitochondrial DNA-related mitochondrial dysfunction in sporadic neurodegenerative diseases. Curr Pharm Des 17:3356-3373

Taivassalo T, Abbott A, Wyrick P, Haller RG (2002) Venous oxygen levels during aerobic forearm exercise: An index of impaired oxidative metabolism in mitochondrial myopathy. Ann Neurol 51:38-44

Taivassalo T, Shoubridge EA, Chen J, Kennaway NG, DiMauro S, Arnold DL, Haller RG (2001) Aerobic conditioning in patients with mitochondrial myopathies: physiological, biochemical, and genetic effects. Ann Neurol 50:133-141

Tanaka M, Takeyasu T, Fuku N, Li-Jun G, Kurata M (2004) Mitochondrial genome single nucleotide polymorphisms and their phenotypes in the Japanese. Ann N Y Acad Sci 1011:7-20

Tang S, Batra A, Zhang Y, Ebenroth ES, Huang T (2010a) Left ventricular noncompaction is associated with mutations in the mitochondrial genome. Mitochondrion 10:350-357

Tang X, Li R, Zheng J, Cai Q, Zhang T, Gong S, Zheng W, He X, Zhu Y, Xue L, Yang A, Yang L, Lu J, Guan MX (2010b) Maternally inherited hearing loss is associated with the novel mitochondrial $tRNA^{Ser(UCN)}$ 7505T> C mutation in a Han Chinese family. Mol Genet Metab 100:57-64

Tarnopolsky MA, Simon DK, Roy BD, Chorneyko K, Lowther SA, Johns DR, Sandhu JK, Li Y, Sikorska M (2004) Attenuation of free radical production and paracrystalline inclusions by creatine supplementation in a patient with a novel cytochrome *b* mutation. Muscle Nerve 29:537-547

Tuppen HA, Blakely EL, Turnbull DM, Taylor RW (2010) Mitochondrial DNA mutations and human disease. Biochim Biophys Acta 1797:113-128

Valente L, Piga D, Lamantea E, Carrara F, Uziel G, Cudia P, Zani A, Farina L, Morandi L, Mora M, Spinazzola A, Zeviani M, Tiranti V (2009) Identification of novel mutations in five patients with mitochondrial encephalomyopathy. Biochim Biophys Acta 1787:491-501

Valnot I, Kassis J, Chretien D, de Lonlay P, Parfait B, Munnich A, Kachaner J, Rustin P, Rötig A (1999) A mitochondrial cytochrome *b* mutation but no mutations of nuclearly encoded subunits in ubiquinol cytochrome c reductase (complex III) deficiency. Hum Genet 104:460-466

Wibrand F, Ravn K, Schwartz M, Rosenberg T, Horn N, Vissing J (2001) Multisystem disorder associated with a missense mutation in the mitochondrial cytochrome *b* gene. Ann Neurol 50:540-543

Zaragoza MV, Fass J, Diegoli M, Lin D, Arbustini E (2010) Mitochondrial DNA variant discovery and evaluation in human Cardiomyopathies through next-generation sequencing. PloS one 2:e12295

Conclusion

In this doctor dissertation, two novel methods have been proposed:

1. We have established the new crossbridge (CB) model based on the molecular mechanisms of ATP-hydrolysis by S1 segment of myosin with the biophysical contraction model and implemented in the simple blood circulation model of cardiovascular system. The new Hybrid model well describes the behavior of CB kinetics with the estimating the energy consumption. The linear relationship between pressure-volume area and the amount of v_{ATPase} per beat are clearly described.
2. The specific technique for diagnosing the mutations in cytochrome *b* gene sequence of mitochondrial DNA that leading to the changes of energy production which is necessary for cardiomyocyte has been developed. This technique provides the high sensitivity and specificity to investigate the mutations at the early stage. Moreover, the development of our study with high resolution melt analysis could provide the fast, reliable, and inexpensive technique to diagnosis the mutations.

Appendix: Model equations

Model equations

- *Dynamics of equivalent crossbridge*

$$X_p = halfSL - h_p \qquad \text{Eq. S1}$$

$$X_w = halfSL - h_w \qquad \text{Eq. S2}$$

$$\frac{dX_p}{dt} = -B_p \cdot \left(h_p - h_{pr}\right) \qquad \text{Eq. S3}$$

$$\frac{dX_w}{dt} = -B_w \cdot \left(h_w - h_{wr}\right) \qquad \text{Eq. S4}$$

$$\frac{dh}{dt} = -B \cdot \left(h - h_r\right) \qquad \text{Eq. S5}$$

- *Calculation of state transitions*

$$Q_1 = Y_b \cdot [M_{DP}(M_T)] \cdot [Ca^{2+}]^{nCa}$$ Eq. S6

$$Q_2 = Z_b \cdot [cM_{DP}]$$ Eq. S7

$$Q_3 = f \cdot [cM_{DP}]$$ Eq. S8

$$Q_4 = g \cdot [cAM_{DPw}]$$ Eq. S9

$$Q_5 = Y_p \cdot [cAM_{DPw}]$$ Eq. S10

$$Q_6 = Z_p \cdot [cAM_{Ds}]$$ Eq. S11

$$Q_7 = Z_d * \cdot [cAM_{Ds}]$$ Eq. S12

$$Q_8 = Z_h \cdot [cAM_T]$$ Eq. S13

$$Q_9 = Z_f \cdot [cM_{DP}(cM_T)]$$ Eq. S14

$$Q_{10} = Y_r \cdot [cAM_{Ds}]$$ Eq. S15

$$Q_{11} = Z_r \cdot [AM_{Ds}] \cdot [Ca^{2+}]^{nCa}$$ Eq. S16

$$Q_{12} = Z_d * \cdot [AM_{Ds}]$$ Eq. S17

$$Q_{13} = Z_h \cdot [AM_T]$$ Eq. S18

- *Differential equations*

$$\frac{d[cM_{DP}]}{dt} = Q_1 - Q_2 - Q_3 + Q_4 \quad \text{Eq. S19}$$

$$\frac{d[cAM_{DPw}]}{dt} = Q_3 - Q_4 - Q_5 + Q_6 + Q_9 \quad \text{Eq. S20}$$

$$\frac{d[cAM_{Ds}]}{dt} = Q_5 - Q_6 - Q_7 - Q_{10} + Q_{11} \quad \text{Eq. S21}$$

$$\frac{d[cAM_{T}]}{dt} = Q_7 - Q_8 \quad \text{Eq. S22}$$

$$\frac{d[cM_{DP}(cM_{T})]}{dt} = Q_8 - Q_9 \quad \text{Eq. S23}$$

$$\frac{dAM_{Ds}}{dt} = Q_{10} - Q_{11} - Q_{12} \quad \text{Eq. S24}$$

$$\frac{d[AM_{T}]}{dt} = Q_{12} - Q_{13} \quad \text{Eq. S25}$$

$$\frac{d[M_{DP}(M_{T})]}{dt} = Q_{13} - Q_1 + Q_2 \quad \text{Eq. S26}$$

- *Rate functions*

$$f = Y_a \cdot e^{-Ra\cdot(halfSL-La)^2} \qquad \text{Eq. S27}$$

$$g = F_h \cdot Y_v \cdot \left(1 - e^{-\gamma\cdot(h_w - h_{wr})^2}\right) + Z_a \qquad \text{Eq. S28}$$

$$F_h = \begin{cases} 0.1 & ; h_w > h_{wr} \\ 1 & ; h_w \le h_{wr} \end{cases} \qquad \text{Eq. S29}$$

$$Z_d{}^* = \frac{Z_d}{\frac{K_{d,ATP}}{[ATP]} \cdot \left(1 + \frac{[ADP]}{K_{d,ADP}}\right) + 1} \qquad \text{Eq. S30}$$

- *ATP rate by contraction*

$$v_{ATPase} = nCa \cdot (Q_7 + Q_{12}) \qquad \text{Eq. S31}$$

$$v_{ATPase} = nCa \cdot \frac{Z_d \cdot ([cAM_{Ds}] + [AM_{Ds}])}{\frac{K_{d,ATP}}{[ATP]} \cdot \left(1 + \frac{[ADP]}{K_{d,ADP}}\right) + 1} \qquad \text{Eq. S32}$$

- *Concentration of myosin S1 segment*

$$[mS1] = [TS] \cdot nCa \qquad \text{Eq. S33}$$

- *Magnitude of contraction*

$$F_b = F_{bw} + F_{bp} \quad \text{Eq. S34}$$

$$F_{bw} = nCa \cdot A_w \cdot [cAM_{DPw}] \cdot h_w \quad \text{Eq. S35}$$

$$F_{bp} = nCa \cdot A_p \cdot ([cAM_{Ds}] + [AM_{Ds}]) \cdot h_p \quad \text{Eq. S36}$$

$$F_p = K_e \cdot (halfSL - hSL_0)^5 + L_e \cdot (halfSL - hSL_0) \quad \text{Eq. S37}$$

- $[Ca^{2+}]$-F_b-v_{ATPase} relationships

$$\ln\left(\frac{V_{\max,Fb}}{F_b} - 1\right) = -n_H \cdot \ln\left(\frac{[Ca^{2+}]}{K_{0.5}}\right) \quad \text{Eq. S38}$$

$$\ln\left(\frac{V_{\max,ATPase}}{v_{ATPase}} - 1\right) = -n_H \cdot \ln\left(\frac{[Ca^{2+}]}{K_{0.5}}\right) \quad \text{Eq. S39}$$

- Ca^{2+} dynamics

$$Q_{rel} = Q_m \cdot \left(\frac{t}{\tau_r}\right)^4 \cdot \exp\left(4 \cdot \left(1 - \frac{t}{\tau_r}\right)\right) + \frac{K_p}{1 + \left(\frac{K_m}{Ca_{rest}}\right)^2} \quad \text{Eq. S40}$$

$$Q_{pump} = \frac{K_p}{1 + \left(\frac{K_m}{[Ca^{2+}]}\right)^2} \quad \text{Eq. S41}$$

$$\frac{d[Ca^{2+}]}{dt} = Q_{rel} - Q_{pump} + (0.3 \cdot nCa \cdot (Q_2 - Q_1 + Q_{10} - Q_{11})) \quad \text{Eq. S42}$$

- *Multi-scale of cardiovascular model*

$$\frac{p_{LV}}{h_{LV}} = \frac{2 \cdot F_{ext}}{r_{LV}} \qquad \text{Eq. S43}$$

$$F_{ext} = K_u \cdot (K_s \cdot F_b + F_p) \qquad \text{Eq. S44}$$

$$h_{LV} = \frac{F_b - F_{bED}}{F_{bES} - F_{bED}} \cdot (h_{LVES} - h_{LVED}) + h_{LVED} \qquad \text{Eq. S45}$$

$$q_0 = \begin{cases} \dfrac{P_{E1} - p_{LV}}{Rpv \cdot K_{rp}} & ; p_{LV} < P_{E1} \\ 0 & ; p_{LV} \geq P_{E1} \end{cases} \qquad \text{Eq. S46}$$

$$q_{in} = \begin{cases} \dfrac{p_{LV} - P_a}{Rlo} & ; p_{LV} > P_a \\ 0 & ; p_{LV} \leq P_a \end{cases} \qquad \text{Eq. S47}$$

$$\frac{dP_a}{dt} = \frac{q_{in} - \dfrac{P_a - P_{E2}}{R_{out}}}{Cds} \qquad \text{Eq. S48}$$

$$\frac{dv_{LV}}{dt} = q_0 - q_{in} \qquad \text{Eq. S49}$$

$$r_{LV} = \left(\frac{v_{LV} - V_\gamma}{K_\beta} \right)^{\frac{1}{K_\alpha}} \qquad \text{Eq. S50}$$

$$halfSL = r_{LV} \cdot K_L + L_b \qquad \text{Eq. S51}$$